ADVANCING EARTH AND SPACE SCIENCES

JGR Oceans

RESEARCH ARTICLE
10.1029/2025JC023554

Preconditioning of Polynya Formation by Ocean Mixing at Maud Rise, Antarctica

Xingchi Wang[1], Alberto C. Naveira Garabato[1], Bieito Fernández Castro[1], Xin Wang[2], Sebastiaan Swart[3,4], Marcel Du Plessis[3], Aditya Narayanan[1], Alessandro Silvano[1], Louis Clément[5], and Margaret Ruth Lindeman[6]

[1]School of Ocean and Earth Science, University of Southampton, Southampton, UK, [2]Qingdao Guoshi Technology Group Co., Ltd, Qingdao, China, [3]Department of Marine Sciences, University of Gothenburg, Gothenburg, Sweden, [4]Department of Oceanography, University of Cape Town, Rondebosch, South Africa, [5]National Oceanography Centre, Southampton, UK, [6]Harvard University, Cambridge, MA, USA

Key Points:

- Widespread interleaving structures are identified along the flank and over the summit of Maud Rise
- Subsurface along-isopycnal heat and salt transports from the flank to the Taylor Cap are approximately 0.18 TW and 4.7×10^3 g kg^{-1} m^3 s^{-1}
- Multiple mixing processes contribute to the preconditioning of the Maud Rise polynya

Correspondence to:

X. Wang,
xingchi.wang@soton.ac.uk

Citation:

Wang, X., Naveira Garabato, A. C., Fernández Castro, B., Wang, X., Swart, S., Du Plessis, M., et al. (2026). Preconditioning of polynya formation by ocean mixing at Maud Rise, Antarctica. *Journal of Geophysical Research: Oceans*, *131*, e2025JC023554. https://doi.org/10.1029/2025JC023554

Received 2 OCT 2025
Accepted 16 JUL 2026

Author Contributions:

Conceptualization: Xingchi Wang, Alberto C. Naveira Garabato, Bieito Fernández Castro
Data curation: Sebastiaan Swart, Marcel Du Plessis
Formal analysis: Xingchi Wang, Xin Wang
Methodology: Xingchi Wang, Bieito Fernández Castro
Project administration: Alberto C. Naveira Garabato
Resources: Sebastiaan Swart, Marcel Du Plessis
Supervision: Alberto C. Naveira Garabato
Validation: Xingchi Wang
Visualization: Xingchi Wang, Xin Wang
Writing – original draft: Xingchi Wang

Abstract

Antarctic open-ocean polynyas trigger vigorous wintertime convection, influencing ocean circulation and atmospheric processes. In the Weddell Sea, interaction between the Weddell Gyre and the Maud Rise seamount generates a Taylor column that favors polynya formation. However, owing to limited observations, the dynamics of such polynya formation remain partially understood, particularly the long-term preconditioning that sets the stage for polynya occurrence. We use glider observations from late austral summer 2022 to investigate the role of mixing in preconditioning, focusing on the interior layer below the pycnocline, which stores heat that melts sea ice and regulates deep convection. We show that multiple mixing processes contribute to the preconditioning. Widespread interleaving structures along the northwestern flank of Maud Rise are identified, indicating that warm, salty water intrudes into the Taylor column along isopycnals. This intrusion is likely driven by lateral shear and eddies, both arising from the flank's anticyclonic circulation. Moreover, eddy shedding, cabbeling, and diffusive convection jointly enhance lateral homogenization and destratification of the Taylor column interior below the pycnocline. Using the large eddy method and a triple decomposition of the tracer variance equation, we calculate snapshot-based along-isopycnal heat and salt transports from the Rise flanks into the Taylor column as ~0.18 TW and ~4.7 $\times$ 10^3 g kg^{-1} m^3 s^{-1}, respectively. At these rates, idealized estimates suggest that polynya-favorable conditions could develop within 2–6 years of the observations. Our results highlight the role of mixing in polynya formation and the need to realistically represent these processes in climate-scale ocean models.

Plain Language Summary

Open-ocean polynyas are areas of open water that form within the sea ice during winter. They allow heat and moisture to escape from the ocean to the atmosphere and induce deep ocean convection, which can affect both atmospheric and ocean circulations. One of the most prominent sites of polynya formation occurs over and around the Maud Rise seamount, located in the Weddell Sea. However, the processes that prepare the ocean for polynya events, known as preconditioning, remain poorly understood because of limited observations. Here, we use data from an autonomous ocean glider deployed around Maud Rise during the late austral summer of 2022 to examine how ocean mixing contributes to preconditioning. We find widespread evidence of warm, salty water from the flanks of Maud Rise intruding into the seamount's overlying cooler and fresher waters along density surfaces, linked to mixing driven by local turbulent currents. Together with other forms of small-scale mixing, this intrusion warms and destratifies the seamount's overlying water, acting to promote polynya formation. Based on glider observations, we quantify the transports of heat and salt and estimate how long the Maud Rise region would take to reach polynya-favorable conditions in response to those transports.

1. Introduction

In the Southern Ocean, polynyas, defined as open water areas within sea ice during winter, play an important role in ocean-atmosphere interactions and deep ocean convection, influencing climate variability and global ocean circulation (Bernardello et al., 2014; Gordon, 2014; Silvano et al., 2023; SO-CHIC consortium et al., 2023; Wadhams, 2014). Polynyas can be categorized as coastal polynyas, primarily maintained by katabatic and along-shelf easterly winds that drive sea ice away from the coast and fast-ice features (Golledge et al., 2025); and open-ocean polynyas, driven by the convection of sensible heat from the upwelling of warm water, occurring far from

Writing – review & editing: Xingchi Wang, Alberto C. Naveira Garabato, Bieito Fernández Castro, Xin Wang, Sebastiaan Swart, Marcel Du Plessis, Aditya Narayanan, Alessandro Silvano, Louis Clément, Margaret Ruth Lindeman

the coast (Gordon, 1991). Open-ocean polynyas have been observed in various regions across the Southern Ocean (Gordon, 1978; Qin et al., 2022; Wei et al., 2022). Among them, the most striking example is the Weddell Sea Polynya (WSP) observed from 1974 to 1976, which reached up to 350,000 km^2 in area and significantly influenced bottom water production and regional heat budgets (Gordon, 1978; Zanowski et al., 2015; Zanowski & Hallberg, 2017; Z. Wang et al., 2017; Spence et al., 2025). Since then, only smaller and more sporadic open-ocean polynyas have occurred in the Weddell Sea, with the most prominent being the 2016/2017 Maud Rise Polynya (MRP, Comiso & Gordon, 1987; Cheon & Gordon, 2019; Campbell et al., 2019). Several studies have suggested that the MRP may serve as a precursor to the WSP, which initially formed over the northeastern flank of Maud Rise before expanding into a much broader area (Cheon & Gordon, 2019; Dufour et al., 2017; Gordon, 1978; Kurtakoti et al., 2018). Understanding the mechanisms behind the MRP formation is therefore critical for improving predictions of open-ocean polynyas in the Weddell Sea. However, predicting the occurrence of the MRP remains challenging, due to the complex ocean-atmosphere-ice interactions implicated in polynya formation.

Maud Rise is a prominent seamount located near 2.5°E, 65°S, embedded within the southern branch of the Weddell Gyre. The seafloor in this region rises sharply from the surrounding Weddell Basin (~5,000 m) to a summit depth of about 1,800 m over approximately 100 km. The Weddell Gyre transports warm and salty Circumpolar Deep Water (CDW) originating from the Antarctic Circumpolar Current (ACC) toward Maud Rise. Due to the Taylor column mechanism (Taylor, 1923), the Maud Rise seamount deflects the gyre around its flanks, thereby isolating the waters over its summit, referred to as the Taylor Cap. Two distinct water masses are observed beneath the Winter Water (WW), a cold interior layer formed by wintertime cooling and mixing (Spira et al., 2024). These water masses are separated by a pronounced density front: the Maud Rise Deep Water (MRDW) within the Taylor Cap, and the Warm Deep Water (WDW) along the flanks of Maud Rise (Beckmann et al., 2001; Brandt et al., 2011; De Steur et al., 2007). In contrast to MRDW, WDW is warmer and saltier, as it represents a modestly modified form of CDW. WDW properties are primarily set by its CDW origin and are further modified along the Weddell Gyre by a range of processes across different scales (Vernet et al., 2019). In winter, WDW upwelling around the seamount's flanks suppresses sea ice formation, leading to a persistent annular region of low sea ice concentration at the edge of Maud Rise, commonly referred to as the warm-water halo (De Steur et al., 2007).

The formation of the MRP is influenced by both short-term triggers (occurring days to weeks prior to polynya formation) and longer-term preconditioning processes (spanning months to years). Short-term triggers can initiate vigorous deep convection that penetrates the pycnocline, bringing warm and salty subsurface water to the surface. This upward heat flux inhibits sea ice formation and facilitates the development of an open-ocean polynya. Several mechanisms have been proposed as potential triggers, including polar cyclones (Campbell et al., 2019; Francis et al., 2019), atmospheric rivers (Francis et al., 2020), thermobaric instabilities (Gülk et al., 2024), and large-scale oceanic eddies (Cheon & Gordon, 2019; Holland, 2001). During polynya formation, associated sea-ice melt may release freshwater at the surface, leading to upper-ocean restratification and potentially shutting down convection and polynya formation (Martinson et al., 1981). In such cases, an additional source of surface density anomalies is required to sustain convection. For instance, during the 2016/2017 MRP event, salt was advected from the Taylor Cap toward the northern flank via Ekman transport, assisting in maintaining deep convection despite the meltwater input (Narayanan et al., 2024). However, without a favorable background state provided by long-term preconditioning, these short-term triggers alone are often insufficient to initiate, sustain, and extend open-ocean polynyas.

Here, we define preconditioning as the set of slow, long-term processes that erode the upper-ocean and interior stratification or accumulate interior heat over Maud Rise. Rather than directly triggering polynya formation, preconditioning primes the oceanic environment for subsequent polynya generation, sustainment, and expansion. For example, during the 2016/2017 MRP, a weakening of the pycnocline was observed ahead of the polynya's onset, likely driven by enhanced upward salt fluxes into the mixed layer associated with persistent anomalies in cyclonic wind stress curl (Campbell et al., 2019; Narayanan et al., 2024). Large-scale climate variability (e.g., the Southern Annular Mode) can modulate upper-ocean salinity by influencing atmospheric conditions, further affecting preconditioning and the likelihood of polynya formation (Cheon et al., 2015; Gordon et al., 2007; Morioka et al., 2024; Silvano et al., 2025; Zhou et al., 2026). Moreover, deep convection linked to preceding polynya events could weaken stratification, contributing to polynya preconditioning (Campbell et al., 2019; Gülk

10.1029/2025JC023554

et al., 2024). However, repeated or prolonged convection can also cool the interior heat reservoir, thereby reducing the upward heat flux needed to suppress sea ice formation and potentially inhibiting future polynyas (Dufour et al., 2017). Therefore, the build-up of the heat reservoir represents another critical component of preconditioning, influencing not only the likelihood of polynya formation but also its duration and spatial extent (Dufour et al., 2017; Rheinlænder et al., 2021). Results from coupled climate models suggest that this accumulation of subsurface heat may occur over multidecadal timescales, driven by both climatic and oceanic circulation variability (Kurtakoti et al., 2018; Martin et al., 2013; van Westen & Dijkstra, 2020).

Despite advances in Earth System Models and regional simulations, reproducing open-ocean polynyas realistically remains difficult. Most models either fail to generate polynyas or produce events that differ markedly from observations in duration, location, and extent (Cheon et al., 2015; Kurtakoti et al., 2018; Mohrmann et al., 2021; Rheinlænder et al., 2021), which may further result in errors in the simulation of the large-scale circulation (Stoessel et al., 2015). These model biases stem from both an insufficient understanding of polynya dynamics and the inadequate representation of key physical processes in climate-scale models. Several studies have highlighted the sensitivity of polynya formation to surface freshwater fluxes and convection parameterizations (e.g., Gülk et al., 2024; Kjellsson et al., 2015; Stoessel et al., 2015).

A better understanding of the dynamics of preconditioning is also important for simulating polynyas. Gülk et al. (2023) suggest that mesoscale eddies may facilitate lateral heat transport into the Taylor Cap across density fronts. Supporting this view, Mohrmann et al. (2022) observe pronounced interleaving structures along the Maud Rise flanks using float measurements, pointing to the intrusion of warm water into the Taylor Cap. Further, previous studies have identified an eastward retroflection along the eastern and northern flanks of Maud Rise, located south of the Weddell Gyre jet and forming an anticyclonic circulation (Cisewski et al., 2011; Gülk et al., 2023). The associated vorticity anomalies may provide an energetic environment favorable for mixing and along-isopycnal intrusions. Other processes such as double-diffusive instability (Mohrmann et al., 2022), thermobaricity (Akitomo, 2006; Gülk et al., 2024; Mohrmann et al., 2021), and cabbeling (Harcourt, 2005) have also been suggested to influence vertical motion and potentially contribute to polynya formation. Nevertheless, the dynamics of ocean mixing and its contribution to preconditioning remain poorly constrained by direct observations.

To address this gap, we analyze a glider data set consisting of multiple cross-sections across the Maud Rise flanks and the Taylor Cap, enabling a systematic investigation of water exchange across the frontal interface. Using the large eddy method and a triple decomposition of the tracer variance conservation equation, we estimate the subsurface lateral exchanges of heat and salt from the Maud Rise's northwestern flank into the Taylor Cap. We also provide observational evidence for mesoscale eddy-driven transport, and suggest a plausible pathway through which mixing contributes to preconditioning. This paper also discusses the potential mechanisms of interleaving structures, Taylor Cap destratification, and the limitations of our results.

2. Methods

2.1. Field Observations and Satellite Data

This study is based on observations from an autonomous underwater glider (Seaglider) during the Southern Ocean Carbon and Heat Impact on Climate (SO-CHIC) project. The glider (SG640) was deployed on the northern flank of Maud Rise on 10 January 2022 and was lost at sea near the eastern Taylor Cap on 7 April 2022, providing 88 days of data and 683 ocean profiles in total. During the mission, it completed seven transects across the northwestern flank and fully traversed the Taylor Cap from west to east (Figure 1a).

Each V-shaped dive cycle of the glider includes a descending and ascending profile of measured temperature, salinity, and pressure for the upper 1,000 m from an unpumped Seabird CT Sail sensor. Raw data were corrected for sensor thermal-lag using the APL-IOP basestation code that applied a first-order thermistor-response lag (Garau et al., 2011). Previous studies suggest that observed interleaving structures typically have horizontal scales of $\mathcal{O}(1–100)$ km, with timescales ranging from days to months (Jakes et al., 2025; Jan et al., 2019). In our observations, the mean horizontal and temporal spacing between consecutive profiles is approximately 1.5 km and 3 hr, respectively. This sampling is therefore sufficient to resolve the dominant interleaving structures and to support the subsequent triple decomposition analysis. Sensor sampling was performed at 0.2 Hz (approximately 0.9 m vertical spacing) in the upper 80 m and at 0.05 Hz (approximately 3 m spacing) below 80 m. Depth-

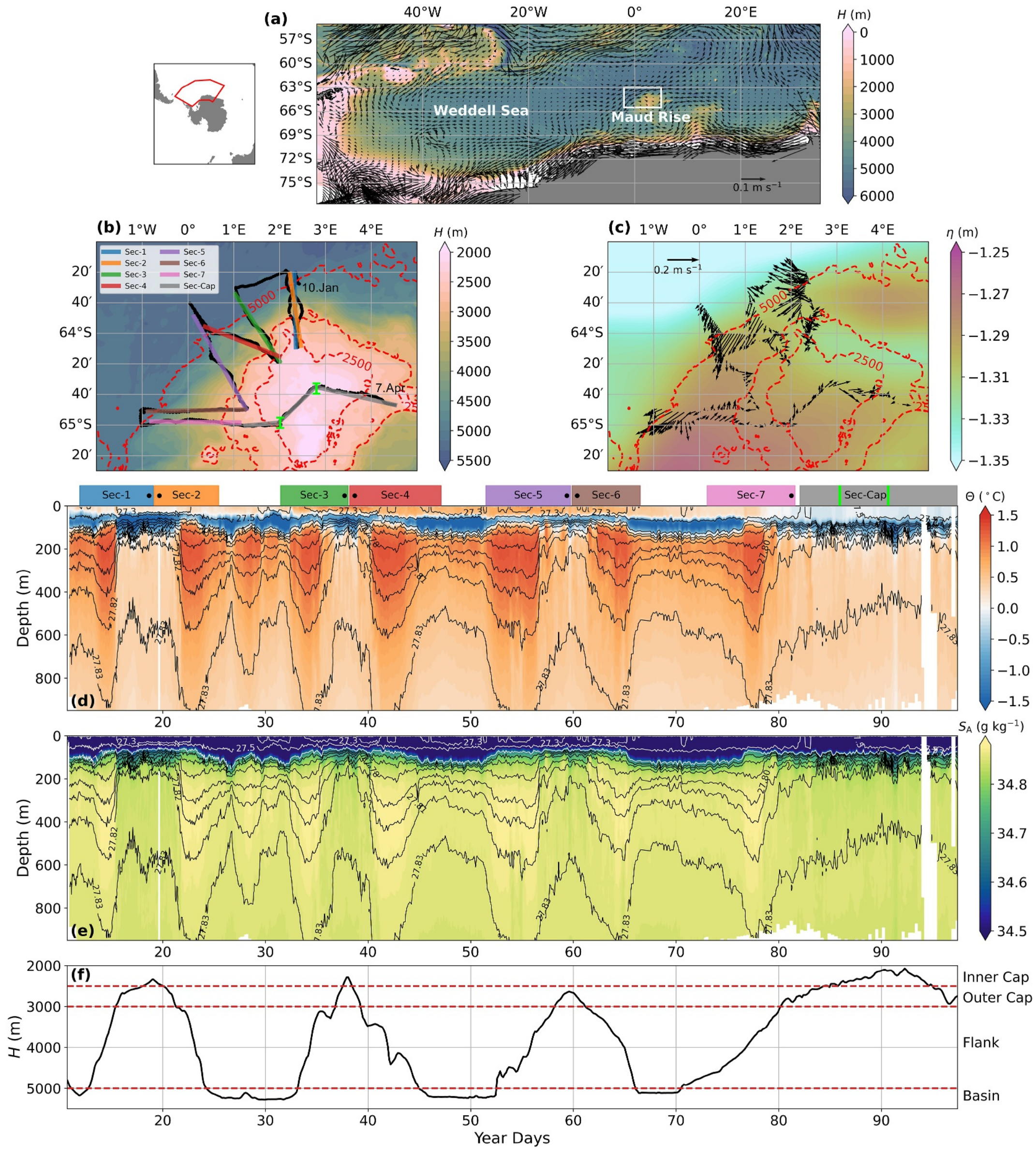

Figure 1. (a) Map of the Weddell Sea region, contextualized relative to Antarctica (left), showing bathymetry, H, and satellite-derived geostrophic currents averaged over the period 2013–2021 (arrows), indicating the Weddell Gyre. The white rectangle denotes the region shown in panels (b) and (c). (b) Map of the glider trajectory over Maud Rise, overlaid on the bathymetry. Dates indicate the start and end of the glider observations. Colored thick lines indicate the seven transects crossing the northwestern flank and the Taylor Cap transect. Vertical I-beam markers divide the Taylor Cap transect of the trajectory into three subsections. (c) Map of depth-averaged velocity vectors estimated from each glider dive, overlaid on absolute dynamic topography from gridded satellite observations averaged over 2013–2021. Dashed contours in (b) and (c) indicate the 2,500-, 3,000-, and 5,000-m isobaths. (d, e) Time series of glider-observed (d) conservative temperature, Θ, and (e) absolute salinity, S_A, with potential density anomaly, σ, overlaid as black and white contours. Colored bars above panel (d) represent the time periods corresponding to the transects shown in (b), with black dots indicating the side of each cross-flank transect close to the Taylor Cap. (f) Bathymetry along the glider trajectory. The three horizontal dashed lines (2,500, 3,000, and 5,000 m) delineate the glider trajectory into four regions, as detailed in Section 3.1.

averaged currents are estimated by comparing the glider's dead-reckoning positioning between consecutive surfacing locations with its true location (Figure 1c). All profiles are vertically interpolated onto a 1 m grid. Each dive or climb profile is assigned a mean time and a geographic position, where the underwater position is linearly interpolated between GPS fixes based on profile time. For cross-transect analysis, hydrographic and velocity data are projected onto fitted transects (Figure 1b), determined using orthogonal least-squares regression of glider positions. The transect-projected data are then interpolated horizontally onto a 1 km grid. We test alternative interpolation methods and find our main results to be insensitive to the interpolation choice.

This study uses the IBCSO Version 2 bathymetry data set (Dorschel et al., 2022b), gridded at a horizontal resolution of 500 m × 500 m. The bathymetry is interpolated onto the glider locations to examine the relationship between ocean properties and seafloor topography.

To quantify mesoscale eddy kinetic energy (EKE) in the vicinity of Maud Rise, we use the gridded sea level anomaly (SLA) and associated geostrophic current product developed by Auger et al. (2022). This data set combines satellite observations from CryoSat-2, Sentinel-3A, and SARAL/AltiKa, and provides horizontal coverage at a resolution of 25 km × 25 km across both open-ocean and sea-ice-covered regions, spanning the period 2013–2021. The EKE is calculated as

$$\mathrm{EKE} = \frac{1}{2}\left(u_{\mathrm{g}}^{\prime 2} + v_{\mathrm{g}}^{\prime 2}\right), \tag{1}$$

where u'_{g} and v'_{g} are the geostrophic current anomalies referenced to the time-mean geostrophic currents over the 2013–2021 period.

2.2. Detection of Interleaving Structures

Spiciness, ς, is used to distinguish different water masses in this study. It is defined as:

$$d\varsigma = \rho(\alpha\, d\Theta + \beta\, dS_{\mathrm{A}}), \tag{2}$$

where ρ is the in situ density, Θ is the conservative temperature, and S_{A} is the absolute salinity. $d\varsigma$, $d\Theta$, and dS_{A} denote the local differentials of spiciness, conservative temperature, and absolute salinity in thermohaline space, respectively. The coefficients α and β represent the thermal expansion and saline contraction coefficients. All variables in Equation 2 are computed using the TEOS-10 Gibbs SeaWater (GSW) Oceanographic Toolbox (McDougall & Barker, 2011).

We also use diapycnal spiciness curvature (DSC), a metric widely utilized to distinguish interleaving structures between different water masses (e.g., Jakes et al., 2025; Jan et al., 2019; Mohrmann et al., 2022; Shcherbina et al., 2009), to examine the thermohaline intrusions between the flank and the Taylor Cap. Diapycnal spiciness curvature is defined as the second derivative of spiciness ς with respect to potential density, expressed as

$$\varsigma_{\sigma\sigma} = \frac{d^2\varsigma}{d\sigma^2}, \tag{3}$$

where σ is the potential density anomaly referenced to the ocean surface. Subscripts of σ denote differentiation with respect to potential density space.

To calculate $\varsigma_{\sigma\sigma}$, we first compute ς in depth space. We then discretize σ into narrow density bins and average ς within each bin to construct the ς profile in σ-space. The curvature $\varsigma_{\sigma\sigma}$ is computed in σ-space following Equation 3. Considering the weak stratification below the pycnocline, we choose a small density bin size of 0.0004 kg m^{-3} to ensure that the depth range corresponding to each density interval remains less than 50 m. The range of σ is set to 27.75–27.84 kg m^{-3}, approximately covering depths below 100 m (Figure 2c). Although the density error associated with the instrumental accuracy, approximately ±0.0025 kg m^{-3}, is larger than the adopted density bin size, our analysis is based on bin-averaged values rather than individual measurements, so random instrumental errors are partly reduced through averaging. Nevertheless, because DSC is highly sensitive to high-frequency noise, residual instrumental errors as well as the standard errors of the bin-averaged spiciness may still generate DSC errors comparable in magnitude to the signal itself. Following Shcherbina et al. (2009), we apply an additional Blackman-windowed moving average with a 15-point window to the binned ς profiles in σ-space to suppress high-frequency noise. Assuming uncorrelated errors between density bins, this smoothing strategy reduces the standard error of the DSC by approximately two orders of magnitude, ensuring a sufficiently large signal-to-noise ratio for robust identification of interleaving structures.

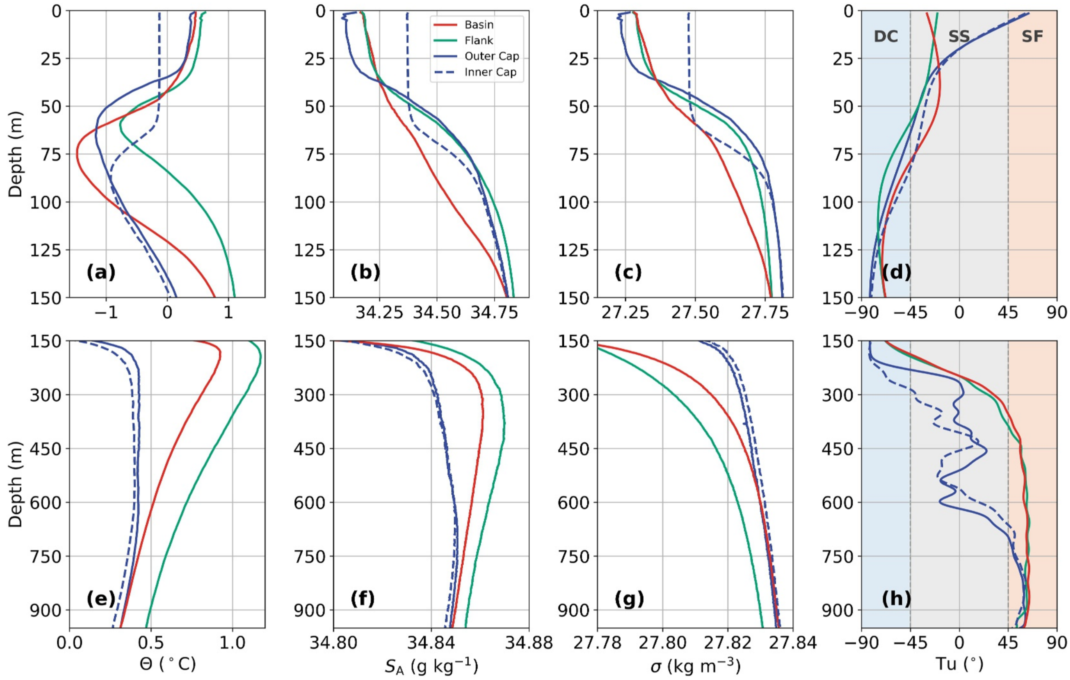

Figure 2. Regional mean profiles of (a, e) conservative temperature, Θ, (b, f) absolute salinity, S_A, (c, g) potential density anomaly, σ, and (d, h) Turner angle, Tu. Panels (a)–(d) show the upper 150 m, while panels (e)–(h) show the 150–950 m depth range. Colored lines represent different regions: Basin (red solid), Flank (green solid), Outer Cap (blue solid), and Inner Cap (blue dashed), as defined in Figure 1f and Section 3.1. Shading in (d, h) indicates the instability regimes based on Tu: diffusive convection (DC, blue), statically stable conditions (SS, gray), and salt fingering (SF, red). Note that the upper and lower panels use different *x*-axis limits for clarity.

To characterize interleaving structures, we follow the approach of Jakes et al. (2025), applying the OpenCV Python package (a machine-learning-based image recognition tool) to identify interleaving features from the $\varsigma_{\sigma\sigma}$ fields. For each transect, the two-dimensional $\varsigma_{\sigma\sigma}$ array is input to OpenCV, which detects regions enclosed by the ±1000 kg m^{-3} contours, representing pronounced interleaving features. Sensitivity tests with different thresholds show that the statistical characteristics and key findings remain robust.

For each detected feature, the length is defined as the horizontal distance between its first and last profiles. By projecting depth onto σ-space, the height is defined as the depth difference corresponding to the minimum and maximum densities across the feature, while the thickness is defined as the mean vertical extent of the interleaving structure across individual profiles. The slope of interleaving structures is estimated using all feature points via orthogonal least squares regression. To reduce noise-induced structures, we only retain features with at least 4 horizontal grid points (4 km). Notably, this approach may also exclude some real interleaving structures, particularly those that intersect the glider track at a large angle. The detected spatial distribution of interleaving should therefore be interpreted with this sampling limitation in mind. When a single interleaving structure contains multiple branches, we retain the branch whose density is most consistent with that of the branching joint.

2.3. Estimating ε From Glider Observations

We estimate the turbulent kinetic energy (TKE) dissipation rate ε from the glider observations using the large eddy method (LEM; Beaird et al., 2012). LEM assumes that ε is proportional to the ratio of TKE ($\sim q^2$) to the overturning timescale ($\sim l/q$), expressed as

$$\varepsilon \sim \frac{q^3}{l}, \tag{4}$$

where q and l represent characteristic turbulent velocity and length scales, respectively. This approximation is based on the assumption that TKE cascades toward smaller scales and ultimately dissipates at the Kolmogorov scale without significant energy loss (Kolmogorov, 1991; Moum, 1996; Tennekes & Lumley, 1972).

Following previous studies (Beaird et al., 2012; Evans et al., 2018; Fernández-Castro et al., 2020), we utilize the Ozmidov length scale $L_o = \sqrt{\varepsilon N^{-3}}$ as the turbulent length scale l, and the vertical velocity fluctuation w' as the turbulent velocity scale q, where N is the buoyancy frequency. This leads to an expression for ε:

$$\varepsilon = c_{\mathrm{E}} N \langle w'^2 \rangle. \tag{5}$$

c_{E} is an empirical constant, and angle brackets $\langle \cdot \rangle$ denote bin-averaging in the vertical coordinate. The buoyancy frequency N and vertical velocity variance $\langle w'^2 \rangle$ are computed in 40-m half-overlapping bins from 20 to 900 m depth. The buoyancy frequency N is calculated by adiabatically sorting the observed density profiles as described in Bray and Fofonoff (1981), representing the background stratification that resists turbulent overturning (Evans et al., 2018). The vertical velocity w is calculated from

$$w = w_{\mathrm{meas}} - w_{\mathrm{model}}, \tag{6}$$

where $w_{\mathrm{meas}} = \partial p/\partial t$ is the measured glider vertical speed, and w_{model} is the predicted glider vertical speed based on a glider flight model using measured pitch, glider buoyancy changes, and seawater density (Frajka-Williams et al., 2011). To isolate turbulent fluctuations, w is high-pass filtered using a fourth-order Butterworth filter to remove low-frequency internal wave signals, denoted as w_{hp}. Following previous studies (Beaird et al., 2012; Evans et al., 2018), we use the larger of N and the frequency associated with a 30-m wavelength as the cutoff frequency. The filtered signal w_{hp} is then detrended by subtracting its bin-averaged mean $\langle w_{\mathrm{hp}} \rangle$ to obtain the vertical velocity fluctuation $w' = w_{\mathrm{hp}} - \langle w_{\mathrm{hp}} \rangle$. Because the flight model assumes steady glider motion, which can be disrupted by control maneuvers such as rolling and pitching, we remove data within a 25-s window after each glider control event and fill the resulting gaps by linear interpolation (Frajka-Williams et al., 2011). For each 40-m bin, bins with more than 20% missing data are excluded from the analysis, and smaller gaps are filled by linear interpolation.

According to Equation 5, estimating ε requires the empirical coefficient c_{E}, which is typically determined by comparing $N\langle w'^2 \rangle$ with microstructure measurements (e.g., Beaird et al., 2012; Evans et al., 2018; Fernández-Castro et al., 2020). However, no concurrent microstructure measurements were available during our observational period. Evans et al. (2018) demonstrate that glider-based dissipation estimates are quantitatively consistent with theoretical scalings within the mixed layer. Motivated by this consistency, we determine c_{E} via the theoretical scaling for mixed-layer turbulence dissipation ε_s, expressed as

$$\varepsilon_{\mathrm{s}} = -\frac{u_*^3}{\kappa_v z} + B_0\left(1 + \frac{z}{h_{\mathrm{ml}}}\right), \tag{7}$$

where the first term represents the contribution from wind-driven shear production, and the second term accounts for the surface buoyancy flux (Gargett, 1989). Here, $\kappa_v = 0.41$ is the von Kármán constant; z is depth (zero at the ocean surface and negative downward); and h_{ml} is the mixed-layer depth, defined as the depth where the potential density exceeds the average value of the top 10 m by 0.03 kg m^{-3}. $u_* = \sqrt{\tau/\rho_0}$ is the friction velocity, where $\tau = \rho_{\mathrm{a}} C_{\mathrm{D}} U_{10}^2$ is the magnitude of wind stress (Figure 3a). $\rho_0 = 1024$ kg m^{-3} and $\rho_{\mathrm{a}} = 1.2$ kg m^{-3} are the reference densities of seawater and air, respectively. C_{D} is the drag coefficient calculated following Large and Pond (1981) and U_{10} is the magnitude of wind speed at 10 m. B_0 is the surface buoyancy flux, given by

$$B_0 = -\frac{g}{\rho_0}\left(\frac{\alpha}{c_{\mathrm{p}}}(Q_{\mathrm{SW}} + Q_{\mathrm{LW}} + Q_{\mathrm{LH}} + Q_{\mathrm{SH}}) + \beta S_{\mathrm{A},0}(P - E)\right), \tag{8}$$

where $g = 9.81$ m s^{-2} is the gravitational acceleration, and c_p is the specific heat capacity of seawater. Q_{SW}, Q_{LW}, Q_{LH}, and Q_{SH} are the shortwave radiation, longwave radiation, latent heat flux, and sensible heat flux,

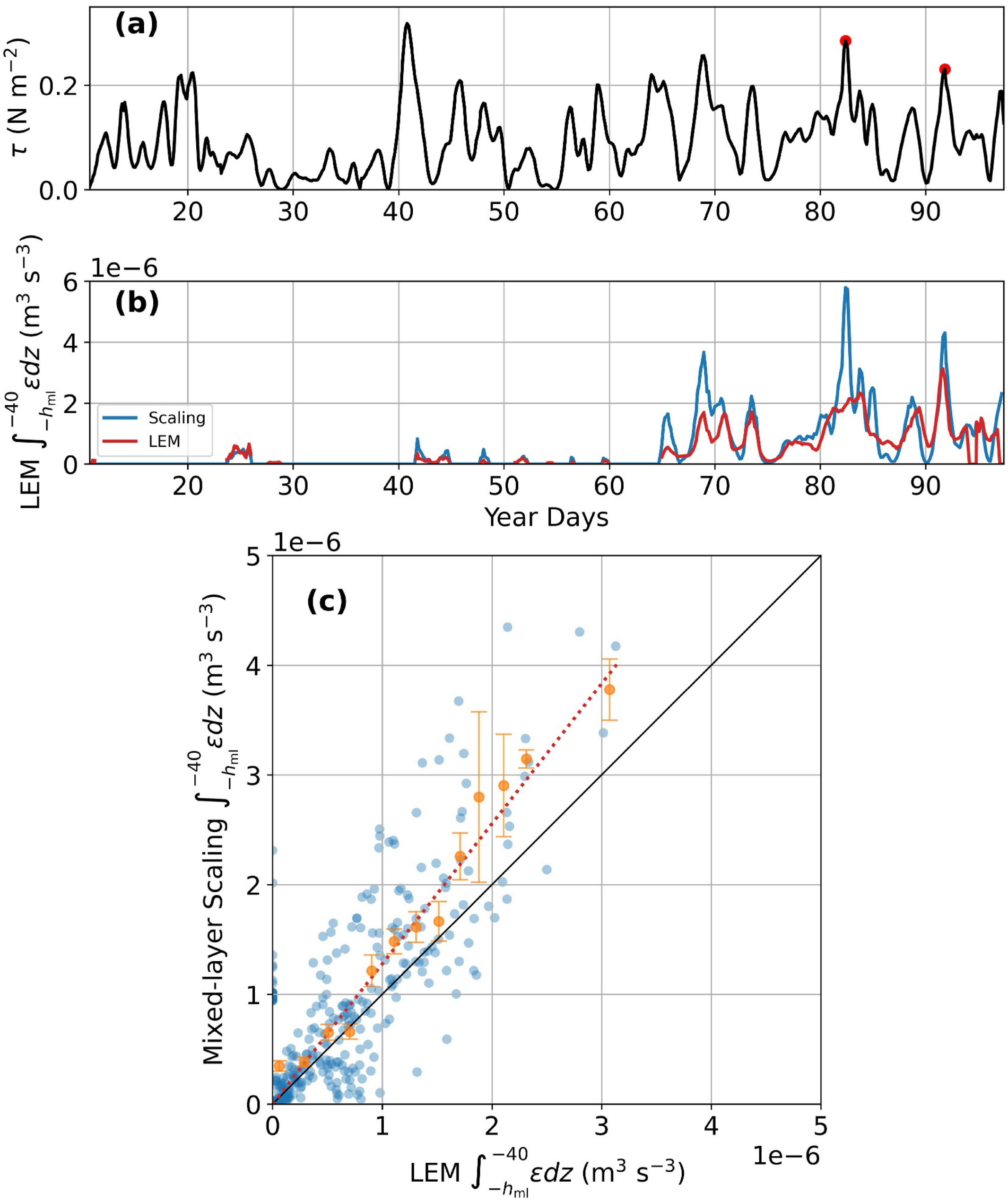

Figure 3. (a) Time series of wind stress derived from the ERA5 data set, sampled at the times and locations of the glider observations. Red dots indicate selected storm events. (b, c) Comparison of the depth-integrated dissipation rate ε estimated from the mixed-layer scaling relation (Equation 7; blue line) and from the glider-derived $N\langle w'^2\rangle$ using LEM (Equation 5; red solid line), shown as (b) a time series and (c) a scatter plot. The values are integrated from 40 m to the mixed-layer depth h_{ml}. Orange dots in (c) indicate bin-averaged values, with error bars representing standard errors. The red dashed line in (c) shows a least-squares linear fit based on the unbinned data points, and the black line denotes $y = x$.

respectively (positive downward, following oceanographic convention). P and E are the precipitation and evaporation rates, and $S_{\mathrm{A},0}$ is the surface absolute salinity. U_{10} and the air–sea flux components used for theoretical scaling are obtained from the ERA5 reanalysis data set (Hersbach et al., 2020).

Given the frequency of glider maneuvers near the surface (Frajka-Williams et al., 2011), only LEM estimates below 40 m are considered reliable. We integrate the glider-derived $N\langle w'^2\rangle$ and the theoretical scaling ε_{s} from 40 m to the base of the mixed layer and find a strong correlation between the two estimates (Figures 3b and 3c). Our results indicate that wind-driven shear turbulence accounts for the majority of the dissipation during the observation period. A linear least-squares fit between the glider-derived $N\langle w'^2\rangle$ and the theoretical scaling ε_s yields $c_E = 1.3 \pm 0.04$, broadly consistent with previous studies, where reported values typically range between 0 and 2 (Moum, 1996; D'Asaro & Lien, 2000; Beaird et al., 2012; Evans et al., 2018).

2.4. Along-Isopycnal Tracer Fluxes

To quantify thermohaline exchanges between the flank and the Taylor Cap, we calculate along-isopycnal tracer fluxes based on glider observations. Following the triple decomposition framework of the tracer variance equation (Fernández-Castro et al., 2020; Ferrari & Polzin, 2005; Garrett, 2001), we separate any tracer field C into three components, expressed as:

$$C = C_\mathrm{m} + C_\mathrm{e} + C_\mathrm{t}, \tag{9}$$

where C_m denotes the large-scale mean (horizontal scales >100 km, vertical scales >100 m, and timescales of months to years), C_e represents mesoscale fluctuations (10–100 km horizontally, 10–100 m vertically, days to months), and C_t captures microscale turbulent fluctuations (scales <10 m, timescales of seconds to hours).

Previous studies (e.g., Ferrari & Polzin, 2005; Garrett, 2001) suggest two primary pathways for tracer variance cascades: (a) direct extraction from the mean state by microscale turbulence (diapycnal pathway), and (b) mesoscale stirring along isopycnal surfaces that generates fine-scale tracer gradients, which are subsequently dissipated by microscale turbulence (isopycnal pathway). Assuming stationarity and local homogeneity, the tracer variance budget can be expressed as:

$$[\mathbf{u}_\mathrm{t} C_\mathrm{t}] \cdot \nabla_\perp C_\mathrm{m} + [\mathbf{u}_\mathrm{e} C_\mathrm{e}] \cdot \nabla_\parallel C_\mathrm{m} = -\frac{1}{2}\chi_C, \tag{10}$$

where $\mathbf{u}$ is the velocity vector, which is also subjected to the triple decomposition. $\chi_C = 2\kappa_C\left[(\nabla C_\mathrm{t})^2\right]$ is the tracer variance dissipation rate, and κ_C is the molecular diffusivity. $\nabla_\perp$ and $\nabla_\parallel$ denote the diapycnal and isopycnal gradient operators, respectively. The brackets $[\cdot]$ indicate an intermediate averaging scale, larger than mesoscale fluctuations but smaller than the mean field variations. The first term in Equation 10 represents the microscale pathway associated with direct turbulent mixing across isopycnals, while the second term corresponds to mesoscale stirring that generates fine-scale tracer gradients along isopycnals. Applying Fick's approximation and approximating the diapycnal gradients as vertical gradients, Equation 10 can be rewritten as:

$$\kappa_\mathrm{dia}\left(\frac{\partial C_\mathrm{m}}{\partial z}\right)^2 + \kappa_\mathrm{iso}|\nabla_\parallel C_\mathrm{m}|^2 = \frac{1}{2}\chi_C, \tag{11}$$

where κ_dia and κ_iso denote the turbulent diapycnal and isopycnal diffusivities, respectively (Ferrari & Polzin, 2005). The first term on the left-hand side corresponds to the diapycnal contribution to $\chi_C/2$, denoted as $\chi_\mathrm{C}^\mathrm{dia}/2$.

Direct estimates of κ_iso and the isopycnal tracer fluxes $[\mathbf{u}_\mathrm{e} C_\mathrm{e}]$ are challenging to assess due to observational limitations. However, as shown in Equation 11, these quantities can be indirectly estimated if κ_dia and χ_C are available. In our study, κ_dia can be estimated using the Osborn method (Osborn, 1980):

$$\kappa_\mathrm{dia} = \frac{\Gamma\varepsilon}{N^2}, \tag{12}$$

where ε and N are based on glider observations, and $\Gamma = 0.2$ is the mixing efficiency. Following Fernández Castro et al. (2024), we estimate the tracer variance dissipation rate χ_C using a Reynolds decomposition approach. The Reynolds decomposition divides the tracer field into a small-scale turbulent component C_t and a non-turbulent component $\overline{C}$, where the overbar denotes an average over scales larger than the turbulent scale but smaller than the mesoscale. Assuming stationarity and homogeneity, the tracer variance budget simplifies to:

$$\overline{\mathbf{u}_{\mathrm{t}} C_{\mathrm{t}}} \cdot \nabla \overline{C} = -\kappa_{\mathrm{dia}} \left(\frac{\partial \overline{C}}{\partial z} \right)^2 = \frac{1}{2} \chi_C. \tag{13}$$

Compared to Equation 11, Equation 13 describes a process in which tracer variance dissipation is locally balanced by microscale turbulence, regardless of whether the tracer variance originates directly from the large-scale mean or is modulated by mesoscale processes. Fernández Castro et al. (2024) compare dissipation estimates based on the Reynolds decomposition with those derived from microstructure measurements, and demonstrate that this assumption holds for temperature variance dissipation.

Therefore, combining Equations 11–13, the along-isopycnal tracer diffusivity κ_{iso} and associated tracer flux $F_{\mathrm{iso}} = [\mathbf{u}_{\mathrm{e}} C_{\mathrm{e}}]$ can be estimated as:

$$\kappa_{\mathrm{iso}} = \frac{\chi_C - \chi_C^{\mathrm{dia}}}{2|\nabla_{\|} C_{\mathrm{m}}|^2} = \frac{\Gamma \varepsilon}{N^2 |\nabla_{\|} C_{\mathrm{m}}|^2} \left(\left(\frac{\partial \overline{C}}{\partial z} \right)^2 - \left(\frac{\partial C_{\mathrm{m}}}{\partial z} \right)^2 \right), \tag{14}$$

$$F_{\mathrm{iso}} = \kappa_{\mathrm{iso}} \nabla_{\|} C_{\mathrm{m}}. \tag{15}$$

In this study, we apply a Blackman-windowed moving average (vertical window of 201 m and horizontal window of 15 km) to the transect-projected tracer profiles to extract the large-scale tracer component C_{m}, and a shorter window (11 m vertical and no horizontal smoothing) to obtain the non-turbulent tracer component $\overline{C}$. The tracer variance dissipation rate χ_{C} and its diapycnal contribution $\chi_{\mathrm{C}}^{\mathrm{dia}}$ are first computed in depth space, and then transformed into σ-space to derive κ_{iso} and the corresponding along-isopycnal fluxes F_{iso}.

3. Results

3.1. Hydrographic Structure and Circulation Patterns

The glider transects across the Maud Rise flank and the entire Taylor Cap enable a detailed investigation of regional hydrographic variability. Consistent with previous studies (e.g., De Steur et al., 2007; Gülk et al., 2023; Mohrmann et al., 2022; Muench et al., 2001), the transects reveal pronounced contrasts in temperature and salinity below the mixed layer (Figures 1d and 1e), which closely align with the bathymetric depth, H (Figure 1f), as noted by Mohrmann et al. (2022). We use H to distinguish the four main oceanographic regions: Basin ($H \geq 5000$ m), Flank ($3000 < H < 5000$ m), Outer Cap ($2500 < H \leq 3000$ m), and Inner Cap ($H \leq 2500$ m). The $H = 2500$ m threshold follows the Taylor Cap boundary definition used by Gülk et al. (2023). Sensitivity tests also confirm that modest adjustments to these bathymetric criteria do not alter the main characteristics of each region.

Figure 2 presents the regional mean profiles of conservative temperature, Θ, absolute salinity, S_{A}, and potential density anomaly, σ. Three vertical layers are identified: the mixed layer (upper ~50 m), the pycnocline (approximately 50–150 m), and the interior layer (roughly below 150 m), each exhibiting distinct hydrographic features.

Among the three layers, the interior layer has the simplest hydrographic structure and dynamics. In all regions, interior Θ remains above 0°C (Figure 2e). The Flank and Basin are occupied by warm, salty WDW, whereas the Cap contains cooler, fresher MRDW (Beckmann et al., 2001; Bersch et al., 1992). Within the Cap, the Inner Cap is slightly colder and fresher than the Outer Cap. The Flank contains the warmest and saltiest WDW (Figures 2e and 2f), consistent with direct supply by the Weddell Gyre from the ACC (Figure 1a). Its shorter flushing timescale likely allows this water to retain more of its original properties, whereas the longer-residing waters in the Basin and Cap are more affected by cooling and mixing. Pronounced temperature and salinity maxima occur in both the Basin and Flank, at about 200 m for Θ and 350 m for S_{A} (Figures 2e and 2f), creating favorable conditions for double-diffusive instability. We use the Turner angle, Tu, to distinguish the instability regime: $45° < \mathrm{Tu} < 90°$ for salt fingering (SF) and $-90° < \mathrm{Tu} < -45°$ for diffusive convection (DC) (Figure 2h), indicating that both types of instability are present in these regions. In contrast, thermohaline maxima are absent in the Cap regions, where vertical gradients of Θ and S_{A} are much weaker (Figure 2g). Below approximately 600 m, hydrographic differences among the four regions diminish significantly (Figures 2e and 2f), consistent with

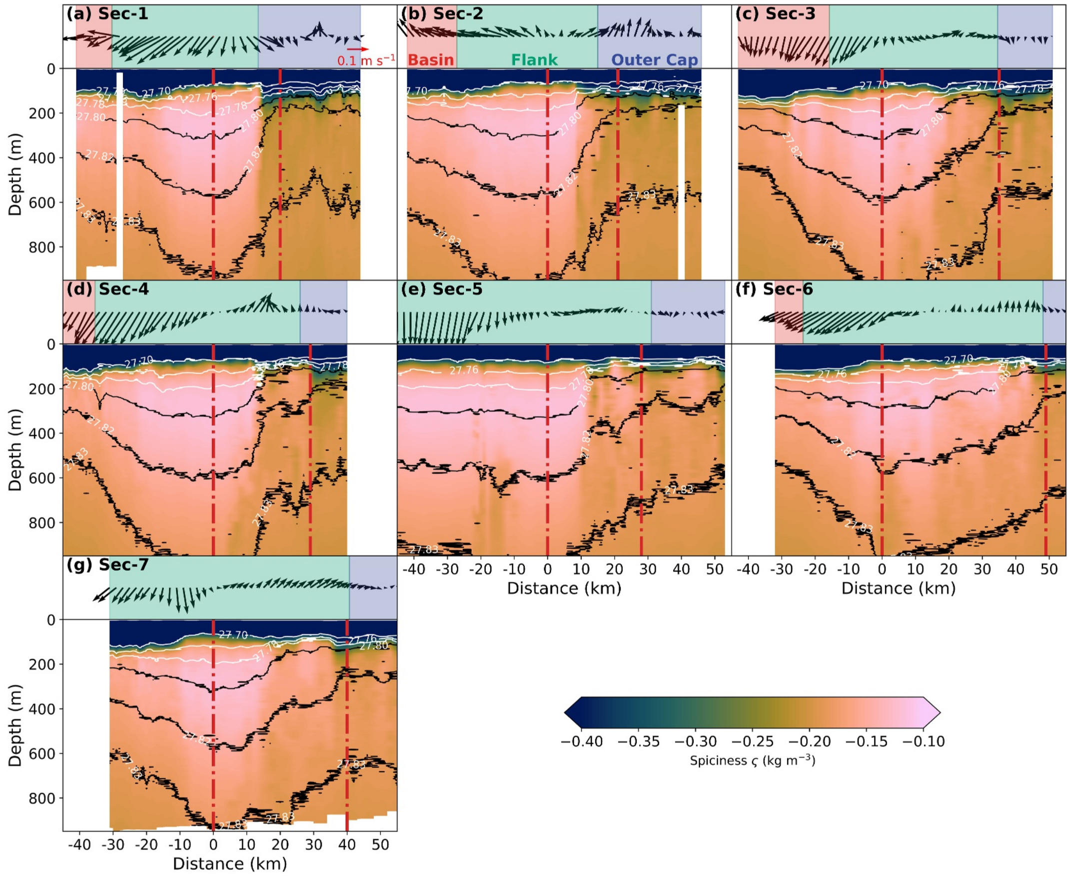

Figure 4. (a)–(g) Glider cross-flank transects (marked in Figure 1b) of spiciness, ς, with potential density anomaly contours overlaid. The top panel in each displays depth-averaged current vectors. Velocity arrows are plotted in geographic directions (up = north and right = east). For each transect, distance of 0 km corresponds to the location of maximum ς, with positive values indicating the direction toward the Taylor Cap. The region between the two vertical red lines marks the Flank–Cap frontal zone, and the colored shading in the top panel denotes the different regions categorized by bathymetric depth, as labeled in (b).

previous profiling-float observations extending to 2000 m (Mohrmann et al., 2022). The contrast in regional variability above and below 600 m is likely due to convection, which cools and homogenizes the upper interior layers but penetrates only weakly into deeper waters.

In the pycnocline, the stratification is salinity-controlled (Figure 2b). Temperature in the pycnocline layer exhibits a concave structure, with a minimum around 70 m that separates summer-warmed surface waters from the underlying WW (Figure 2a). Below this minimum, temperature rapidly increases, indicating a transition to WDW or MRDW, which also suggests a diffusive-convection regime (Figure 2d). Consistent with the interior layer, the Flank has the warmest and saltiest pycnocline. However, the pycnocline structure in the Basin and Outer Cap differs from the pattern of the interior layer. The Outer Cap pycnocline is as salty as that of the Flank and distinctly saltier than that of the Basin by up to 0.2 g kg^{-1}. It is also warmer than the Basin at 70–100 m by about 0.5 °C. This salty and warm Outer Cap pycnocline arises from the steep isopycnals between the Flank and Outer Cap, which enable the warm, salty WDW in the Flank (150–600 m) to intrude upward into the Outer Cap pycnocline (Figure 4). In contrast, the isopycnals between the Flank and Basin are flatter, limiting such exchange.

In contrast to the pycnocline and interior layers, the properties of the mixed layer are primarily influenced by temporal changes in atmospheric forcing during the glider period. This is evident in the colder and saltier mixed layer observed over the Inner Cap region (Figures 2a and 2b), where profiles were collected after late March, when enhanced surface cooling triggered convection and entrainment of saltier water from below.

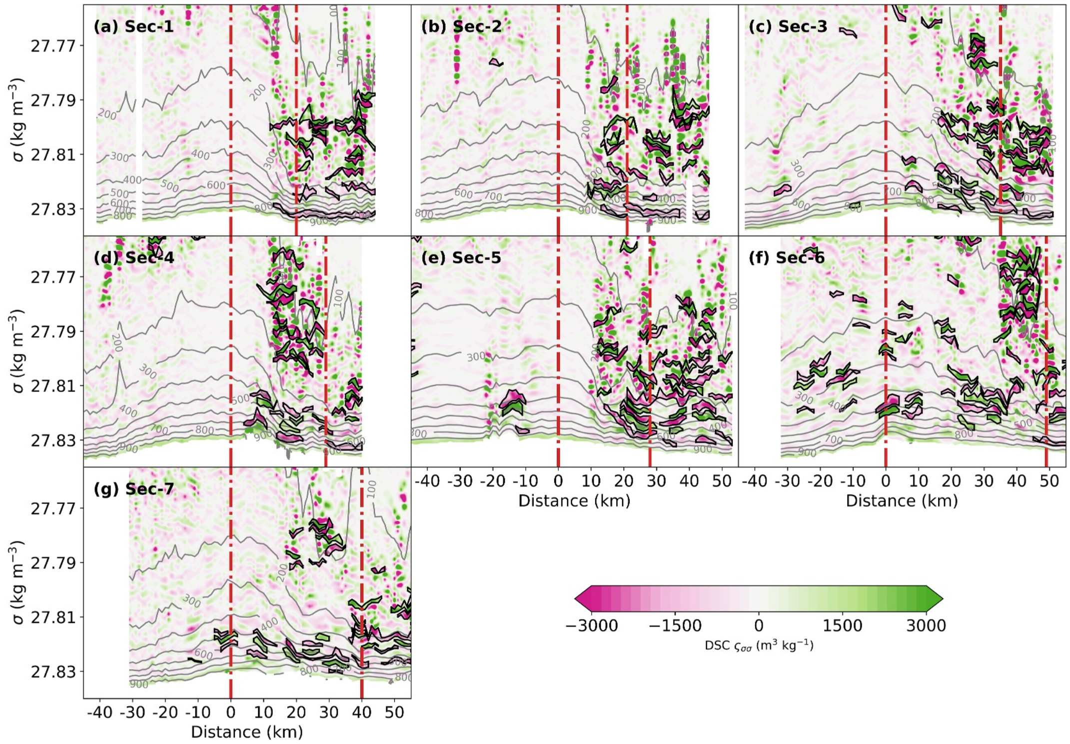

Figure 5. DSC, $\varsigma_{\sigma\sigma}$, of seven cross-flank glider transects (marked in Figure 1b), plotted in σ-space. Color shading indicates diapycnal spiciness curvature (DSC) values, with interleaving structures highlighted by thick black contours, identified using the $\pm 1{,}000\ \mathrm{m^3\ kg^{-1}}$ threshold on DSC (see Methods). Gray contours denote depth projected onto σ-space. The vertical lines and horizontal axes are identical to those in Figure 4.

Glider-derived depth-averaged velocities show an anticyclonic circulation along the Flank, consistent with previous observations and modeling studies (Cisewski et al., 2011; Gülk et al., 2023). This circulation is characterized by a southwestward flow over the northwestern part of the Flank region (approximately following the 5000-m isobath) and a northeastward return flow over the southeastern part of the Flank region (approximately following the 3000-m isobath; Figure 1c). This observed anticyclonic circulation suggests barotropic dominance, because the horizontal density gradients shown in Figure 1d would instead be expected to favor a cyclonic baroclinic circulation. This barotropic dominance is further supported by the elevated absolute dynamic topography over the Flank region (Figure 1c), consistent with the modeling results of Gülk et al. (2023).

3.2. Water Mass Exchange Between Flank and Taylor Cap: Interleaving Structures

As shown in Figures 1d and 1e, distinct hydrographic properties emerge along isopycnals between the Flank and Outer Cap. Previous float observations have identified interleaving structures in this region (Mohrmann et al., 2022), indicating the intrusion of surrounding waters into the Taylor Cap. Here, we characterize the spatial structure and variability of the interleaving structures based on the glider observations.

To accurately quantify the interleaving features, we further define a Flank–Cap frontal zone (marked by vertical lines in Figure 4) using the isopycnal slope, rather than relying on a rough division based on bathymetric depths. The frontal boundary on the Flank side is defined as the location of largest spiciness, and the boundary on the Cap side is taken as the location where the isopycnal slopes of 27.80–27.82 kg m^{-3} decrease to 5% of their maximum. The width of the frontal zone varies between approximately 20 and 50 km across different transects, and is narrower toward the northern flank (upstream) and broader toward the western flank (downstream). Across these cross-flank transects (Transect 1 to Transect 7), subsurface isopycnals tilt sharply upward at the Flank–Cap fronts, with markedly larger horizontal spiciness contrasts (Figure 4). Pronounced isopycnal vertical displacements (~50–100 m) occur primarily within the Flank–Cap frontal zone, particularly at the interface between the main southwestward flow and the northeastward retroflection (Figure 4).

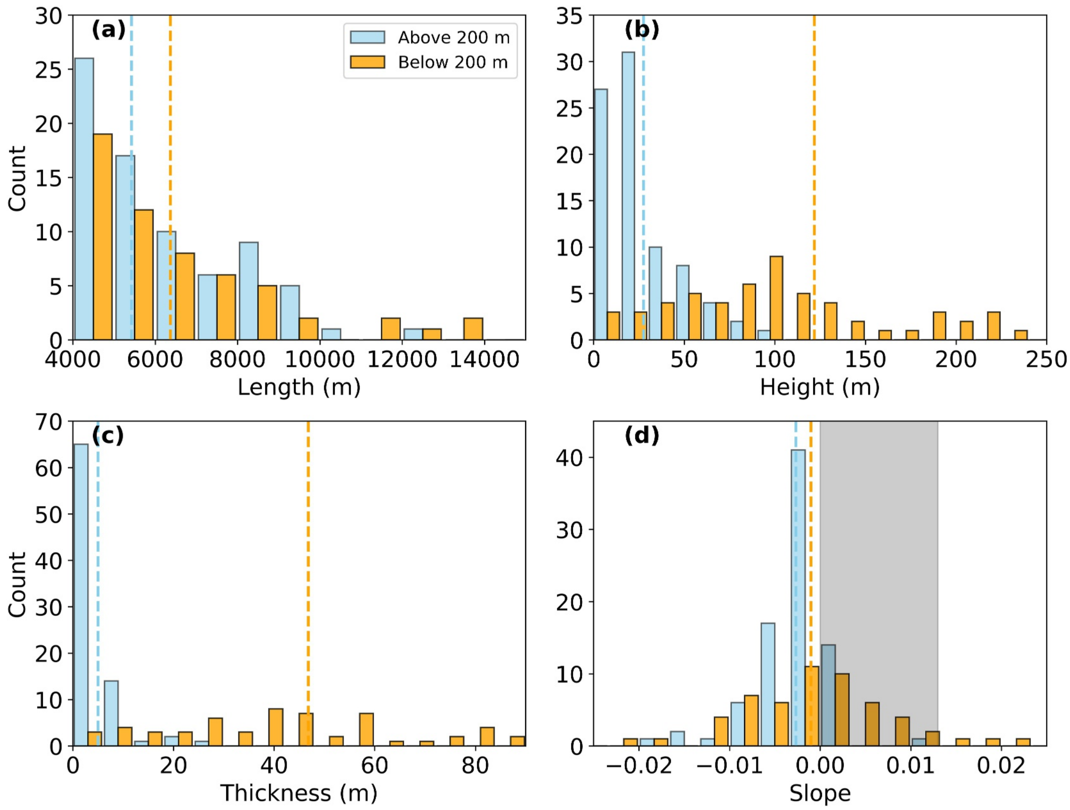

Figure 6. Statistical distribution of interleaving structure characteristics detected in the Flank–Cap frontal zones: (a) horizontal length, (b) vertical height, (c) thickness, and (d) feature slope in depth coordinate, analyzed for above (blue) and below (yellow) 200 m depth. The plotting ranges are truncated to better show the main distributions; the excluded tails contain only sparse extreme values. Vertical dashed lines indicate mean values for each group. The shaded area in panel (d) indicates the theoretical slope criterion based on May and Kelley (1997), discussed in detail in Section 4.1.

To investigate the thermohaline variability and water mass exchanges over the Maud Rise, we examine the DSC over the cross-flank transects (Figure 5). As expected, DSC profiles show consistently elevated values in the Flank–Cap frontal zones across all transects (Figure 5), indicating robust interleaving and enhanced lateral water mass exchange. In contrast, the frontal zones between the Flank and Basin regions (i.e., negative distance in Figures 4 and 5) exhibit weaker DSC due to more homogeneous hydrographic conditions along isopycnals. Several large DSC values are also observed in these zones, which may reflect interleaving structures or subsurface-intensified eddies (Testor et al., 2018).

Figure 6 summarizes the geometric properties of the interleaving structures identified in Figure 5 using a DSC threshold of $\pm 1{,}000\ \mathrm{m^3\ kg^{-1}}$, including their length, height, layer thickness, and slope (defined in Section 2.2). We categorize the statistics into upper and lower layers separated at $z = -200$ m. Although the length of interleaving structures is similar in both layers ($\sim$6 km), their vertical height and thickness differ markedly. Below 200 m, interleaving structures have mean vertical heights and thicknesses of 121 and 46 m, both much larger than those above 200 m, where the corresponding values are 27 and 5 m (Figures 6b and 6c). These structures in the lower layer also exhibit correspondingly steeper slopes (Figure 6d). The slope of interleaving structures has been widely used to infer their underlying generation mechanisms (Beal, 2007; Shcherbina et al., 2009; Jan et al., 2019), which are discussed in Section 4.1.

Elevated DSC values are also found well within the Taylor Cap region (Figure 7), particularly in the top 200 m. Such elevated DSC likely indicates active mixing processes, and is unexpected under the presumed isolation of a Taylor column. Storm events may account for some high-DSC observations, as most measurements within the Taylor Cap were collected in late autumn, when the mixed layer was relatively deep and wind stress was elevated

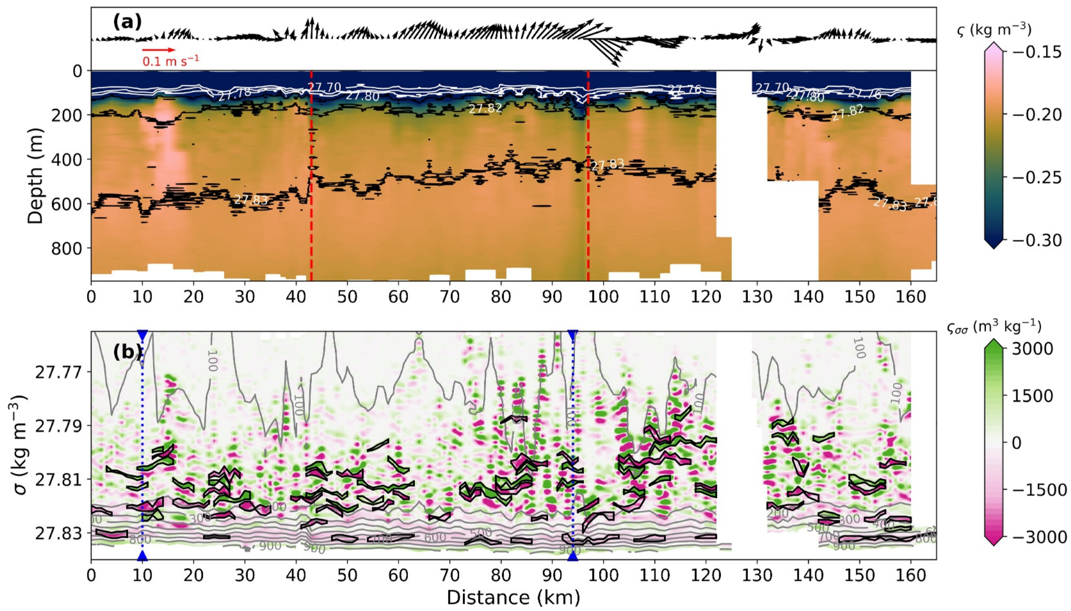

Figure 7. (a) Glider depth-averaged velocity and spiciness, ς, for Sec-Cap (Figure 1b), similar to Figure 4. (b) DSC, $\varsigma_{\sigma\sigma}$, for Sec-Cap, similar to Figure 5. The horizontal axis represents distance, with zero denoting the location of the western side of Sec-Cap. Vertical red dashed lines in (a) indicate the connection points between the three segments of the transect, which follow different compass directions, as marked by the light green I-beam symbols in Figure 1b. Vertical blue lines indicate the storm events, corresponding to the dots in Figure 3a.

(Figures 3a and 7). The weak stratification in the interior layer of the Taylor Cap may also favor the downward penetration of surface-driven stirring.

Mesoscale eddies are another likely contributor. Mean-state EKE, calculated from satellite-derived geostrophic current anomalies over 2013–2021, is higher over the Flank than over both Cap regions (Figure 8). This is consistent with the glider-derived velocity field (Figure 1c), which shows strong lateral shear in the Flank,

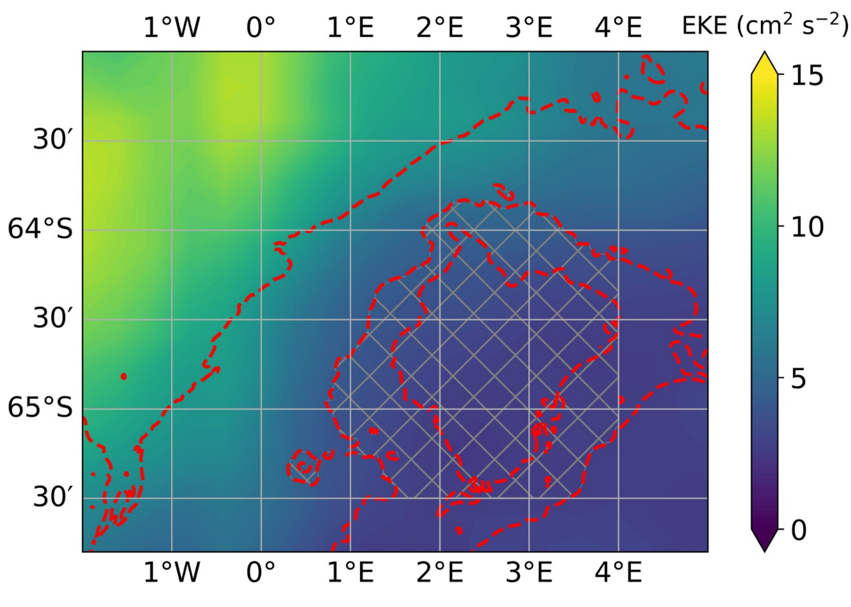

Figure 8. Mean-state eddy kinetic energy from satellite-derived geostrophic current anomaly during the period of 2013–2021 (see Methods). Red contours indicate 5,000-, 3,000-, and 2,500-m isobaths, as in Figures 1b and 1c. Hatched area represents the Taylor Cap region used in the timescale calculation.

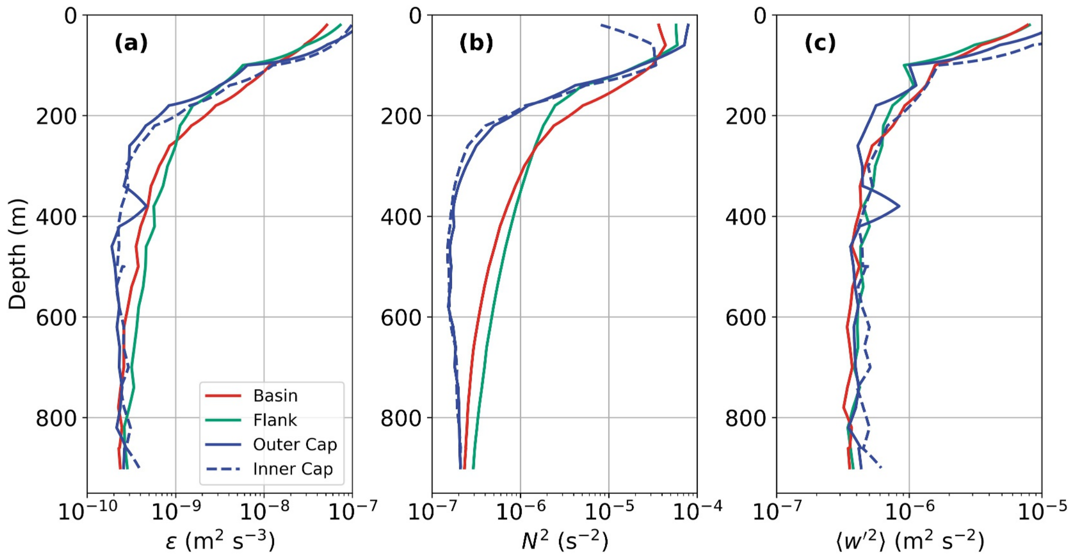

Figure 9. Regional mean profiles of (a) glider-derived turbulent dissipation rate ε, (b) buoyancy frequency squared N^2 calculated from adiabatically sorted density profiles, and (c) glider-derived vertical velocity variances $\langle w'^2 \rangle$. Colored lines represent different regions, same as Figure 2.

suggesting favorable conditions for mesoscale eddy generation. Nonetheless, some of these eddies may penetrate into the Taylor Cap and contribute to the active mixing inferred there, as suggested by previous modeling results (Gülk et al., 2023). Consistent with this possibility, the glider observations reveal several eddy-like features within the Taylor Cap. These features are characterized by spicier subsurface water masses (e.g., near 15 and 140 km in Figure 7), together with cyclonic circulation and thermocline doming, both of which are consistent with mesoscale eddies. Such features may represent eddies shed from the Flank region, although contributions from non-annular structures, such as meanders or filamentary intrusions, cannot be ruled out. However, given their spatial separation and the likely mixing and dissipation during propagation, filaments alone are unlikely to explain the thermohaline anomalies observed in the central Taylor Cap. We therefore interpret these features as primarily eddy-associated, while allowing for some contribution from non-annular processes.

As these eddy-associated features propagate inward, the weak stratification within the Taylor Cap allows exchange between the eddy-carried warm, salty waters and the cold, fresh ambient MRDW, giving rise to interleaving structures (Figure 7). This continual exchange progressively reduces the thermohaline signatures of the eddies as they move inward. Due to the dilution of eddy-carried water masses, the Taylor Cap exhibits a spatial pattern with warmer and saltier waters in the Outer Cap and relatively colder and fresher waters in the Inner Cap (Figures 1d, 1e, 2e and 2f).

3.3. Turbulent Tracer Fluxes Along Isopycnals

To quantify the Flank–Cap lateral transfers, we estimate the along-isopycnal fluxes of heat, $Q_{\mathrm{iso}} = \rho_0 c_{\mathrm{p}} F_{\Theta}^{\mathrm{iso}}$, and salt, $F_{S_{\mathrm{A}}}^{\mathrm{iso}}$, based on glider observations. Before calculating these turbulent fluxes, we first investigate the regional vertical structure of the glider-derived turbulent dissipation rate ε, which is largest near the surface ($\sim 10^{-8}$ m^2 s^{-3}) and decreases with depth to $\sim 10^{-10}$ m^2 s^{-3} (Figure 9a), consistent with previous measurements by Shaw and Stanton (2014). Within the upper 100 m, regional differences in ε are minor. The Inner Cap shows slightly elevated ε, primarily due to enhanced $\langle w'^2 \rangle$ likely driven by surface cooling-induced convection (Figure 9). Below 100 m, N becomes the dominant control on ε, with larger values observed in the Flank and Basin. In contrast, $\langle w'^2 \rangle$ exhibits no significant regional differences at these depths (Figure 9).

Using the estimated ε, we compute the along-isopycnal diffusivity κ_{iso} and the associated heat and salt fluxes via Equations 14 and 15. As our focus is on isopycnal transport into the Cap's interior layer, the analysis is conducted within the σ range of 27.78–27.835 kg m^{-3}, using density bins of 0.0004 kg m^{-3}. During the calculation, Transect 6 shows an anomalous peak in diffusivities and fluxes at $\sigma = 27.825$ kg m^{-3}, due to local negative along-

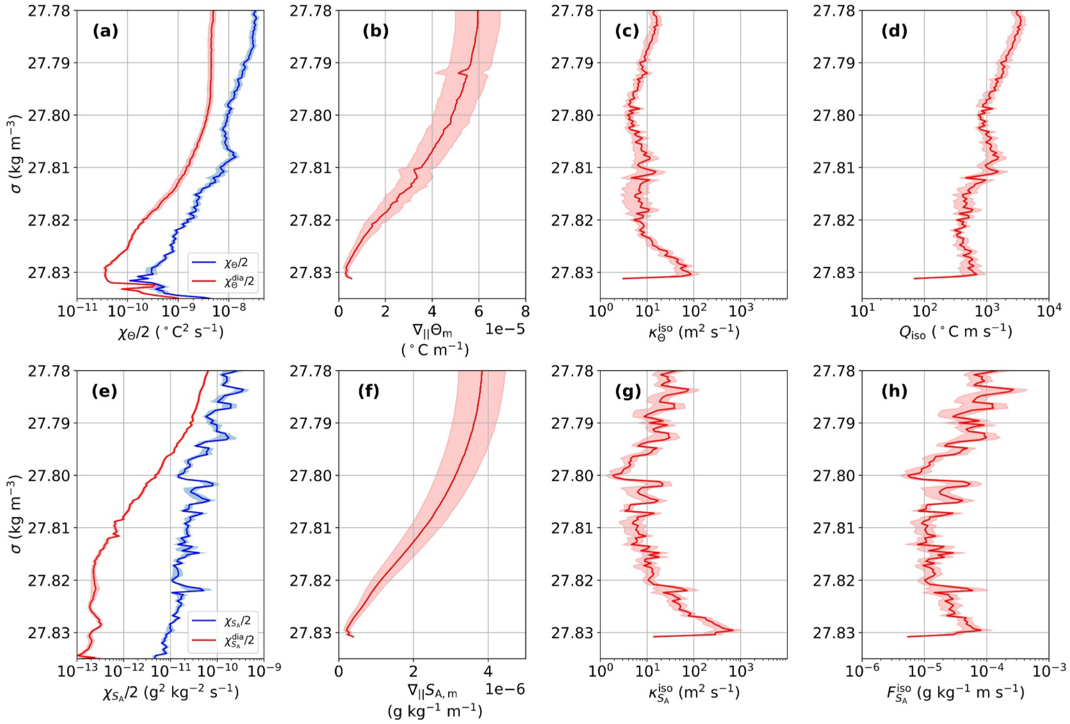

Figure 10. Profiles averaged over the Flank–Cap frontal zones in σ-space across all cross-flank transects except Transect 6: (a) turbulent dissipation rate of conservative temperature variance, χ_Θ, (blue) and its diapycnal component, $\chi_\Theta^{\mathrm{dia}}$, (red); (b) along-isopycnal gradient of large-scale background conservative temperature, $\nabla_{\|}\Theta_{\mathrm{m}}$; (c) along-isopycnal heat diffusivity, $\kappa_\Theta^{\mathrm{iso}}$; and (d) along-isopycnal heat flux, Q_{iso}. Panels (e)–(h) show the corresponding quantities for absolute salinity. The shaded areas represent the standard error across these cross-flank transects.

isopycnal gradients. Because this spurious peak would bias our subsequent estimation, we exclude Transect 6 from the calculation (Figure 10).

The transect-averaged dissipation of temperature variance, χ_Θ, exceeds its diapycnal counterpart, $\chi_\Theta^{\mathrm{dia}}$, by approximately an order of magnitude across the entire σ range, indicating the dominance of fine-scale along-isopycnal processes below 150 m (Figures 10a–10d). The estimated along-isopycnal heat diffusivity, $\kappa_\Theta^{\mathrm{iso}}$, generally ranges from 10^1 to 10^2 m^2 s^{-1}, with peak values found between 27.82 and 27.83 kg m^{-3} (approximately 550–900 m and 200–600 m at the Flank and Cap boundaries of the frontal zones, respectively). Leach et al. (2011) use a multiple regression method based on station profiles and derive isopycnal diffusivities of 70–140 m^2 s^{-1} in this region, also reporting larger values at higher σ levels in broad agreement with our results. Moreover, our values closely match the eddy diffusivity from an idealized model introduced by Klocker and Abernathey (2014), lending further credibility to our diagnostics.

In contrast to χ_Θ, the dissipation rate of salinity variance, χ_{S_A}, exceeds its diapycnal component $\chi_{S_A}^{\mathrm{dia}}$ by about an order of magnitude for $\sigma > 27.80$ kg m^{-3}, but is more comparable within the 27.78–27.80 kg m^{-3} range. This agreement at lower densities likely arises because stratification in this layer is primarily salinity-controlled, causing isopycnals to align closely with isohalines. As a result, along-isopycnal salinity gradients are weak, and diapycnal mixing dominates χ_{S_A}. In contrast, temperature plays a lesser role in determining density and exhibits greater along-isopycnal variability, leading to a stronger isopycnal contribution to χ_Θ. The along-isopycnal salt diffusivity $\kappa_{S_A}^{\mathrm{iso}}$ closely matches $\kappa_\Theta^{\mathrm{iso}}$ in both vertical structure and magnitude. Although we expect $\kappa_{S_A}^{\mathrm{iso}} = \kappa_\Theta^{\mathrm{iso}}$ under ideal conditions, the observed offsets are most likely due to the estimation of χ. Specifically, the salinity variations are smaller than temperature variations, making them more susceptible to measurement noise and leading to greater deviation in χ_{S_A}. Nevertheless, the close agreement between the two diffusivities supports the robustness of our diffusivity estimates.

Assuming $\kappa^{\mathrm{iso}} = \left(\kappa^{\mathrm{iso}}_{S_\mathrm{A}} + \kappa^{\mathrm{iso}}_{\Theta}\right)/2$, we calculate Q_{iso} and $F^{\mathrm{iso}}_{S_\mathrm{A}}$ within the Flank–Cap frontal zones using the transect-averaged κ^{iso} and isopycnal gradients. Vertically integrating the along-isopycnal fluxes within the σ-range of 27.78–27.835 kg m^{-3} yields a depth-integrated heat flux of $(4.5 \pm 0.14) \times 10^5$ W m^{-1} and a salt flux of $(8.1 \pm 0.25) \times 10^{-3}$ g kg^{-1} m^2 s^{-1}, in which the errors come from the uncertainties in c_E. Integration of the mean depth-integrated fluxes along the northern and western flanks of the Taylor Cap (400 km) results in along-isopycnal transports of ∼0.18 TW in heat and $\sim 4.7 \times 10^3$ g kg^{-1} m^3 s^{-1} in salt into the 150–700 m layer of the Taylor Cap. Our estimated heat transport is broadly consistent with the 11-year model simulations of Gülk et al. (2023), which show that the lateral heat flux from the flank to the Taylor Cap ranges from 0 to 0.3 TW within the 200–1,000 m depth range. This consistency suggests that mixing-driven along-isopycnal transport is a dominant contribution to the warming of the Taylor Cap interior layer.

In addition, we predict the approximate timescale for the next polynya formation by considering an idealized scenario in which the heat is entirely retained within a horizontally homogeneous Taylor Cap. As the maximum temperature in the Taylor Cap interior layer can exceed 0.8°C prior to polynya formation (Gülk et al., 2023), we construct a hypothetical temperature profile with 0.8°C at 250 m, decreasing linearly to the glider-observed temperatures at 150 and 950 m. By comparing this artificial profile with the glider-observed mean temperature profile over the Taylor Cap, we estimate that an additional 1.6×10^{19} J of heat would be required to bring the 150–700 m depth range of the Taylor Cap region (hatched region in Figure 8) to the artificial conditions. Given the estimated lateral flux, the heat reservoir could be established over a period of approximately 4 years following the time of observation, assuming no heat loss to the WW layer. Since the observations are 5 years after the last polynya event, which consumed the heat previously stored in the interior layer over the Taylor Cap, this estimate suggests that the heat-recharge timescale for MRP is on the order of ∼10 years. However, this timescale should be regarded as a first-order estimate, as it is subject to uncertainties associated with multiple factors, which we discuss further in Section 4.3.

4. Discussion

4.1. Driving Mechanisms of Interleaving Structures

Here, we evaluate the observations within the context of existing theoretical frameworks to provide insight into processes that may drive the interleaving structures observed at Maud Rise. The mechanisms of thermohaline interleaving are usually categorized into two broad theoretical views: active theories, which suggest that interleaving structures form spontaneously by extracting energy from the thermohaline field through double-diffusive instabilities (Ruddick & Kerr, 2003; May & Kelley, 1997, 2001); and passive theories, which attribute the formation of structures to pre-existing thermohaline gradients that are stretched and reorganized by mesoscale eddies (Ferrari & Polzin, 2005; Smith & Ferrari, 2009).

May and Kelley (1997) introduce a theoretical threshold for the maximum cross-frontal slope of salt-fingering-driven interleaving under linear instability. This criterion is commonly used to assess whether observed interleaving structures may originate from active double-diffusive processes. Specifically, the slope s_i of salt-fingering intrusions is expected to lie between 0 and the critical slope, s^*_i, defined as:

$$s^*_\mathrm{i} = \frac{\epsilon_z s_\mathrm{S} + s_\sigma}{\epsilon_z + 1}, \quad \epsilon_z = \left(1/\gamma_f\right)/(R_\rho - 1). \tag{16}$$

$s_\mathrm{S} \equiv S^{\mathrm{m}}_{\mathrm{A},x}/S^{\mathrm{m}}_{\mathrm{A},z}$ and $s_\sigma \equiv \sigma^{\mathrm{m}}_x/\sigma^{\mathrm{m}}_z$ are the cross-front slopes of large-scale background isohalines and isopycnals, respectively; the superscript m represents large-scale components, and the subscripts x and z indicate partial derivatives; $\gamma_f = 0.5$ is the temperature-salt flux ratio for SF, typically ranging from 0.4 to 0.8; and $R_\rho = 4$ is the mean density ratio within our salt-fingering regime. We assume that the along-transect gradient approximates the cross-front gradient and calculate s_S and s_σ within the Flank–Cap frontal region below 200 m for each cross-flank transect except Transect 6. Using the transect-mean gradients, we estimate the theoretical critical slope to be $s^*_i = 0.013$. Figure 6d shows that observed slopes span both positive and negative values, many of which fall outside this theoretical bound, suggesting that the interleaving structures are not solely driven by salt-finger instability. Similar discrepancies between theory and observations have been reported in previous studies (Beal, 2007; Kuzmina et al., 2005).

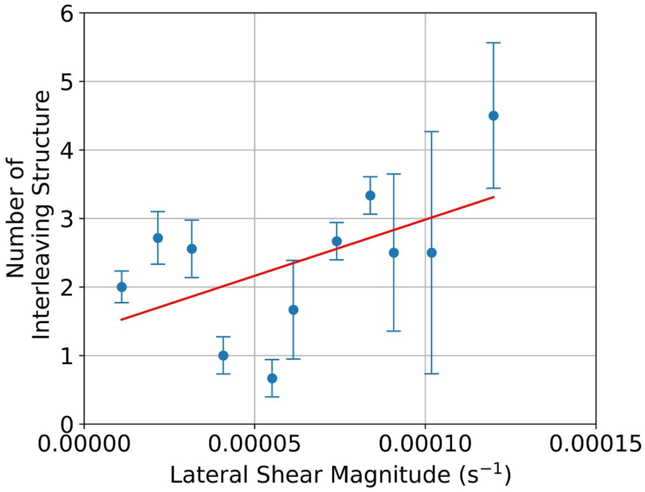

Figure 11. Relationship between interleaving structure occurrence and lateral shear magnitude in the Flank–Cap frontal zones of all cross-flank transects below 200 m. Each zone is divided into overlapping 9 km segments (50% overlap), and the lateral shear magnitude is calculated from glider-derived depth-averaged velocities within each segment. The number of interleaving structures detected in each segment is counted, and the resulting data are binned by lateral shear magnitude with a bin size of 10^{-5} s^{-1}. The *y*-axis shows the mean number of interleaving structures within each shear bin, with error bars indicating standard deviation. The red line represents the linear fit to the binned data.

Figure 11 shows that the frequency of interleaving occurrences in this regime (below 200 m) is positively correlated with lateral shear strength in the Flank–Cap frontal zone. This supports the interpretation that the observed structures may result from passive stirring and stretching of background thermohaline gradients by horizontal shear. According to quasi-geostrophic stirring theory, the geometry of tracer filaments is controlled by the ratio of vertical shear to horizontal strain, which implies a slope of order f/N (Smith & Ferrari, 2009). Based on the spatially averaged observed stratification in the Flank–Cap frontal zone below 200 m, we estimate f/N to range from 0.08 to 0.25. Our observed interleaving slopes remain well below this range, indicating substantially flatter structures than the steepest slopes expected under strong mesoscale eddy tilting. This is likely because mesoscale eddies are too weak to strongly tilt the interleaving structures. Although frontal density gradients and the horizontal shear associated with the anticyclonic flow can, in principle, generate mesoscale eddies, the observed eddy velocity scales are much smaller than the background barotropic current. This suggests that mesoscale eddy stirring is weak, and that barotropic horizontal shear is likely the primary driver of the observed interleaving. Previous studies also suggest that barotropic horizontal shear can efficiently stretch thermohaline gradients into layered interleaving structures (Ferrari & Polzin, 2005; Ruddick et al., 1999).

In contrast to the salt-fingering regime (approximately below 300 m over the Flank region, as shown in Figure 2h), interleaving structures within the diffusive-convection regime (above 200 m) exhibit smaller thickness and vertical extent (Figure 6). This is likely because stratification is strong at those depths, which inhibits the vertical development of interleaving structures and makes their dynamics more difficult to interpret within either the active or passive theoretical frameworks.

The interleaving structures observed in the Cap regions are exceptionally thick (>100 m), exhibit slopes smaller than f/N, and frequently occur in the statically stable regime ($-45° < \mathrm{Tu} < 45°$). Given these atypical characteristics and the relatively weak EKE there, it is unlikely these features were generated locally by active SF or vigorous mesoscale stirring. Rather, they more plausibly represent advected relic structures formed upstream, or quasi-steady, slowly restructured features resulting from weak stirring within the Taylor Cap region itself. The weak stratification here further supports this interpretation, as it allows the persistence of broad, diffusive layering structures, consistent with previously reported advective and slowly evolving interleaving features observed in weakly stratified oceanic environments (Ferrari & Polzin, 2005).

4.2. Destratification of the MRDW Layer

As described in Section 3.1, WDW intrudes isopycnally into the shallow depths of the Outer Cap. When this intrusion mixes with colder, fresher waters, such as the overlying WW, it becomes denser due to the nonlinear equation of state, a process known as cabbeling. The resulting dense water then sinks to its equilibrium depth, producing a persistent downward density flux (McGraw et al., 2025). This downward density flux erodes the stratification within the MRDW layer, making it more prone to deep-reaching convection during polynya formation. Diffusive convection also contributes to MRDW densification, as temperature anomalies equilibrate faster than salinity, leaving behind saltier and denser remnants (Schmitt, 1994). Unlike cabbeling, this mechanism does not rely on turbulent mixing and can operate continuously. While these processes lead to the densification of MRDW, they simultaneously enhance the stratification between the WW and MRDW layers, as reported by Harcourt (2005). The presence of warm-water-carrying eddies within the Taylor Cap interior suggests that both cabbeling and DC likely operate throughout the Cap region. Together, these processes may promote widespread destratification and contribute to polynya preconditioning.

From the glider-derived density profile over the Taylor Cap, we estimate that an additional 1.4×10^{11} kg of mass is required to destratify the layer of 150–700 m across the Taylor Cap (hatched region in Figure 8). For the linear equation of state, $\alpha F_{\Theta}^{\mathrm{iso}} = \beta F_{S_A}^{\mathrm{iso}}$ is required along an isopycnal. For the nonlinear equation of state, however, variations in α and β prevent this relation from holding everywhere. To focus on the cabbeling effects on the Cap side of the Flank–Cap frontal zone, we assume $\alpha_f F_\Theta^{\text{iso}} = \beta_f F_{S_A}^{\text{iso}}$ on the Flank side and therefore construct two balanced flux pairs: (a) F_Θ^{iso} and $F_{S_A,\text{bal}}^{\text{iso}}$; and (b) $F_{\Theta,\text{bal}}^{\text{iso}}$ and $F_{S_A}^{\text{iso}}$. F_Θ^{iso} and $F_{S_A}^{\text{iso}}$ are our calculated fluxes based on observations, while $F_{S_A,\text{bal}}^{\text{iso}} = \alpha_f F_\Theta^{\text{iso}}/\beta_f$ and $F_{\Theta,\text{bal}}^{\text{iso}} = \beta_f F_{S_A}^{\text{iso}}/\alpha_f$ are balance-based pseudo-fluxes derived from their paired observed fluxes. α_f and β_f represent the thermal expansion and haline contraction coefficients on the Flank side of the Flank–Cap frontal zone (i.e., the left red vertical lines in Figure 4), averaged over all cross-flank transects.

Using the values of α and β on the Cap side of the flank–Cap frontal zone (i.e., the right red vertical lines in Figure 4), denoted as α_c and β_c, we then compute density fluxes as $-\alpha_c F_\Theta^{\text{iso}} + \beta_c F_{S_A,\text{bal}}^{\text{iso}}$ and $-\alpha_c F_{\Theta,\text{bal}}^{\text{iso}} + \beta_c F_{S_A}^{\text{iso}}$. After vertical and horizontal integration, the resulting effective mass transports are 850 and 610 kg s^{-1} along the northern and western flanks. Based on their mean value, we estimate that complete destratification of the Cap could occur in roughly 6 years. In practice, part of the heat is likely lost to the overlying WW, while most of the salinity remains in the Cap through cabbeling or DC. Neglecting the compensation from heat transport yields an idealized lower-limit timescale of ~2 years. Both timescales are comparable to the timescale of Cap warming (~4 years), suggesting that the build-up of the interior heat reservoir and the destratification of the Cap likely occur on similar timescales. Unlike the recharge–discharge behavior of the Taylor Cap heat reservoir, polynya-associated convection likely further disrupts the stratification within the Taylor Cap. Here, we estimate only the timescale required to reach a stratification state favorable for polynya formation, whereas the subsequent evolution and recovery of stratification after polynya onset remain uncertain and require further observations.

4.3. Limitations in Transport Estimates

The estimation of along-isopycnal heat and salt transports in this study relies on several key assumptions that may introduce uncertainties, highlighting the need for more comprehensive observations in this region.

First, due to the lack of direct microstructure measurements, along-isopycnal tracer fluxes are derived from estimated tracer variance dissipation rates, which assume a balance between dissipation and production via microscale turbulent stirring. Although we cannot directly validate this approach in our study region, Fernández Castro et al. (2024) find good agreement between Osborn–Cox estimates and microstructure observations, within a factor of 2 across five orders of magnitude. Additionally, our estimated dissipation rate of temperature variance χ_Θ aligns with previously published microstructure values of $\sim 10^{-8}$ K^2 s^{-1} beneath the WW thermocline (Shaw & Stanton, 2014).

Second, the diapycnal diffusivity κ_{dia} is inferred from glider-based turbulent dissipation, which requires calibration against microstructure observations. In the absence of co-located microstructure data, we apply a mixed-layer-based scaling approach that has been validated at a site in the North Atlantic subtropical gyre (Evans et al., 2018). However, the comparison with mixed-layer scaling is limited to the 40–100 m range to exclude unreliable glider estimates, where sparse sampling may introduce uncertainty in the correction coefficient c_E.

Finally, the estimated heat and salt fluxes represent a single glider deployment during austral summer–fall and do not capture temporal variability. The Weddell Gyre exhibits substantial seasonal and interannual changes (Campbell et al., 2019; Fahrbach et al., 2004; Neme et al., 2021), which likely modulate the along-isopycnal transport. Storm forcing may also exert a transient influence on the flux estimation. Therefore, our flux estimates should be viewed as a snapshot rather than a long-term mean. The estimated timescale of polynya preconditioning should also be interpreted as a reference value conditioned on the observed 2022 hydrographic state, rather than a universal estimate, as both the fluxes and the background stratification of the Taylor Cap may vary across different years.

Taken together, these limitations underscore the need for sustained observational efforts in the MRP formation region. Future studies incorporating co-located microstructure data, higher-frequency sampling, and broader spatial coverage will be essential to validate and refine isopycnal transport estimates and their role in shaping ocean stratification at Maud Rise.

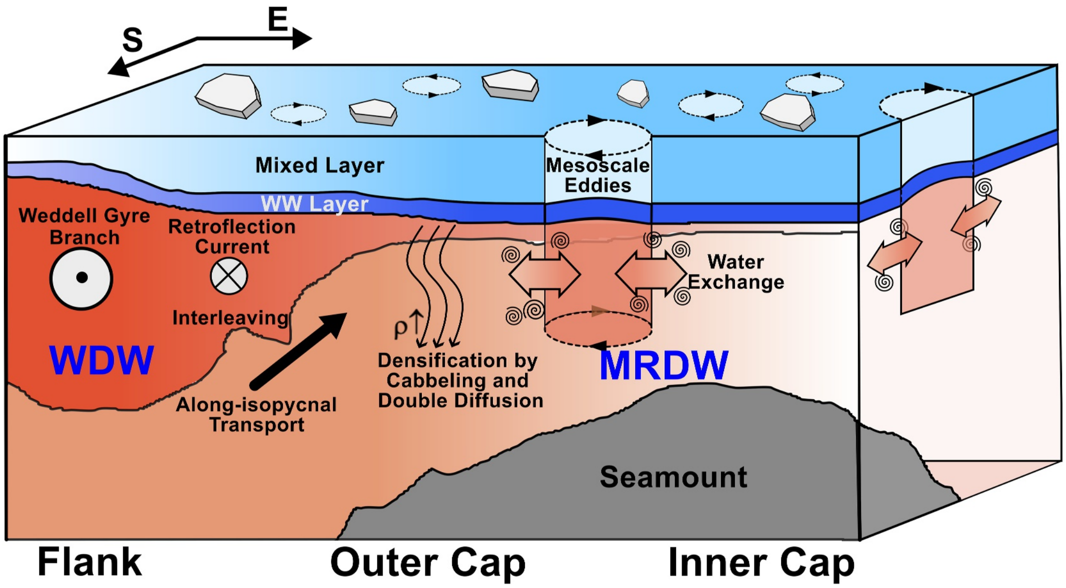

Figure 12. Schematic illustrating how ocean mixing preconditions Maud Rise polynya formation through warming and destratification of the Taylor Cap interior.

5. Conclusions

Using glider observations spanning multiple transects across the northwestern flank of Maud Rise and the Taylor Cap, we investigate the role of ocean mixing in the long-term preconditioning of the Maud Rise Polynya. Consistent with previous studies (De Steur et al., 2007; Mohrmann et al., 2022; Muench et al., 2001), the glider observations reveal strong hydrographic contrasts between the warm, salty flank and the colder, fresher Taylor Cap, separated by steep density fronts closely linked to local topography. Glider-derived depth-averaged velocities confirm a previously identified anticyclonic circulation along the northwestern flank, composed of the southwestward Weddell Gyre jet and a northeastward retroflection, indicating barotropic dominance.

Pronounced interleaving structures are observed in the Flank–Cap frontal zones and are primarily driven by lateral shear. We also identify unexpected properties within the Taylor Cap interior, including interleaving features and mesoscale eddy activity. These observations suggest that the Taylor Cap may be less dynamically isolated and more variable than traditionally assumed, and that lateral exchange and transient atmospheric forcing may help shape its internal structure.

These findings outline a mixing-driven pathway for Taylor Cap preconditioning, summarized schematically in Figure 12. Anticyclonic circulation along the flank generates an energetic environment prone to enhanced lateral shear instabilities and eddy generation. This energetic environment enables flank-sourced WDW to be transported along isopycnals into the shallower depths of the Taylor Cap outer boundary, where it interacts with the overlying WW. Cabbeling and DC can densify this upwelled flank-sourced WDW, causing it to sink and erode the upper MRDW stratification. In addition, eddies shed from the flank can carry either this modified water or flank-sourced WDW directly into the Taylor Cap interior, where their mixing further warms and salinifies the surrounding MRDW. Cabbeling and DC may also occur during eddy transport, leading to densification and destratification of the upper MRDW in the inner Taylor Cap. These processes produce a warmer, less stratified MRDW layer, thereby preconditioning the region for polynya formation.

Using the large eddy method and a triple decomposition of the tracer variance equation, we quantify an along-isopycnal heat transport of ~0.18 TW and a salt transport of $\sim 4.7 \times 10^3$ g kg^{-1} m^3 s^{-1} from the flank into the Taylor Cap based on our snapshot observations. Together with cabbeling, DC, and mesoscale eddies within the Taylor Cap, these transports promote warming and stratification erosion in the Taylor Cap interior layer. Based on the snapshot-derived transport estimates, we compute idealized timescales for the Taylor Cap to reach polynya-favorable conditions from the 2022 observed state: about 4 years for heat content and 2–6 years for destratification. However, it should be noted that such preconditioning within the Taylor Cap does not by itself guarantee polynya formation, which still requires short-term triggers. Moreover, historical polynyas have often opened over the northern flank of Maud Rise, suggesting that the local oceanic and sea-ice conditions there cannot be overlooked in understanding polynya formation. The processes identified here should therefore be viewed as part of the broader oceanic preconditioning and modulation of the Maud Rise polynyas, rather than as a complete explanation of their initiation.

Since the rapid sea-ice retreat in 2016, Antarctic ice extent has remained low, with several recent years reaching record minima (Parkinson, 2019; Purich & Doddridge, 2023). Concurrently, upper-ocean salinity has increased since 2015 (Silvano et al., 2025). Under these evolving climate conditions, the inaccurate representation of polynyas in climate-scale ocean models could amplify biases in climate projections, given the polynyas' impacts on large-scale oceanic and atmospheric circulations (Broecker et al., 1999; Z. Wang et al., 2017; Mohrmann et al., 2021; Zhou et al., 2023; Ayres et al., 2024). By identifying the role of ocean mixing in polynya preconditioning, this study improves our understanding of the mechanisms governing polynya formation, and points to the importance of credibly modeling the mixing processes discussed herein.

Conflict of Interest

The authors declare no conflicts of interest relevant to this study.

Availability Statement

The Seaglider (SG640) data used in this study are available at https://doi.org/10.5281/zenodo.15228200 (Swart et al., 2025). The IBCSO Version 2 bathymetry data set is available at https://doi.org/10.1594/PANGAEA.937574 (Dorschel et al., 2022a). Atmospheric forcing was obtained from ERA5 hourly data, available at https://cds.climate.copernicus.eu/datasets/reanalysis-era5-single-levels-timeseries (Copernicus Climate Change Service, 2025). The gridded SLA product is available from AVISO+ at https://doi.org/10.24400/527896/a01-2022.010 (AVISO+, 2022). The code used for data processing and figure generation in this study is available at https://doi.org/10.5281/zenodo.19810990 (X. Wang, 2026).

Acknowledgments

X.W., A.C.N.G., S.S. and M.d.P. are supported by the European Union's Horizon 2020 research and innovation program SO-CHIC project (no. 821001). Additional support for X.W. and A.C.N.G. comes from the U.K. Natural Environment Research Council (NERC) DEFIANT project (NE/W004747/1). A.C.N.G. further acknowledges U.K. Research and Innovation guarantee funding for a European Research Council Advanced Grant (EP/X025136/1). S.S. receives funding from a Wallenberg Academy Fellowship (WAF 2015.0186). B.F.C. is supported by a European Research Council's Consolidator Grant (REMIX-TUNE, 101169952), and by an Advanced Research and Invention Agency's Forecasting Tipping Points Grant (POLEMIX, SCOP-PR01-P021). A.S. acknowledges funding from NERC (NE/V014285/1). We thank all the glider pilots involved and the R/V SA Agulhas II captain, crew, and technicians for their support in the glider deployment. We are also grateful to the three anonymous reviewers for their constructive comments and insightful suggestions.

References

Akitomo, K. (2006). Thermobaric deep convection, baroclinic instability, and their roles in vertical heat transport around maud rise in the Weddell Sea. *Journal of Geophysical Research*, *111*(C9), C09027. https://doi.org/10.1029/2005jc003284

Auger, M., Prandi, P., & Sallée, J.-B. (2022). Southern Ocean sea level anomaly in the sea ice-covered sector from multimission satellite observations. *Scientific Data*, *9*(1), 70. https://doi.org/10.1038/s41597-022-01166-z

AVISO+. (2022). Gridded and along-track sea level heights and geostrophic currents – Antarctic [Dataset]. https://doi.org/10.24400/527896/a01-2022.010

Ayres, H. C., Ferreira, D., Park, W., Kjellsson, J., & Ödalen, M. (2024). A comparison of the atmospheric response to the Weddell Sea polynya in atmospheric general circulation models (Agcms) of varying resolutions. *Weather and Climate Dynamics*, *5*(2), 805–820. https://doi.org/10.5194/wcd-5-805-2024

Beaird, N., Fer, I., Rhines, P., & Eriksen, C. (2012). Dissipation of turbulent kinetic energy inferred from seagliders: An application to the eastern nordic seas overflows. *Journal of Physical Oceanography*, *42*(12), 2268–2282. https://doi.org/10.1175/jpo-d-12-094.1

Beal, L. M. (2007). Is interleaving in the agulhas current driven by near-inertial velocity perturbations? *Journal of Physical Oceanography*, *37*(4), 932–945. https://doi.org/10.1175/jpo3040.1

Beckmann, A., Timmermann, R., Pereira, A. F., & Mohn, C. (2001). The effect of flow at maud rise on the sea-ice cover–numerical experiments. *Ocean Dynamics*, *52*(1), 11–25. https://doi.org/10.1007/s10236-001-8173-5

Bernardello, R., Marinov, I., Palter, J. B., Galbraith, E. D., & Sarmiento, J. L. (2014). Impact of Weddell Sea deep convection on natural and anthropogenic carbon in a climate model. *Geophysical Research Letters*, *41*(20), 7262–7269. https://doi.org/10.1002/2014gl061313

Bersch, M., Becker, G. A., Frey, H., & Koltermann, K. P. (1992). Topographic effects of the maud rise on the stratification and circulation of the weddell gyre. *Deep-Sea Research, Part A: Oceanographic Research Papers*, *39*(2), 303–331. https://doi.org/10.1016/0198-0149(92)90111-6

Brandt, A., Bathmann, U., Brix, S., Cisewski, B., Flores, H., Göcke, C., et al. (2011). Maud Rise–A snapshot through the water column. *Deep Sea Research Part II: Topical Studies in Oceanography*, *58*(19–20), 1962–1982. https://doi.org/10.1016/j.dsr2.2011.01.008

Bray, N. A., & Fofonoff, N. (1981). Available potential energy for mode eddies. *Journal of Physical Oceanography*, *11*(1), 30–47. https://doi.org/10.1175/1520-0485(1981)011<0030:apefme>2.0.co;2

Broecker, W. S., Sutherland, S., & Peng, T.-H. (1999). A possible 20th-century slowdown of Southern Ocean deep water formation. *Science*, *286*(5442), 1132–1135. https://doi.org/10.1126/science.286.5442.1132

Campbell, E. C., Wilson, E. A., Moore, G. K., Riser, S. C., Brayton, C. E., Mazloff, M. R., & Talley, L. D. (2019). Antarctic offshore polynyas linked to southern hemisphere climate anomalies. *Nature*, *570*(7761), 319–325. https://doi.org/10.1038/s41586-019-1294-0

Cheon, W. G., & Gordon, A. L. (2019). Open-ocean polynyas and deep convection in the southern ocean. *Scientific Reports*, *9*(1), 6935. https://doi.org/10.1038/s41598-019-43466-2

Cheon, W. G., Lee, S.-K., Gordon, A. L., Liu, Y., Cho, C.-B., & Park, J. J. (2015). Replicating the 1970s' weddell polynya using a coupled ocean-sea ice model with reanalysis surface flux fields. *Geophysical Research Letters*, *42*(13), 5411–5418. https://doi.org/10.1002/2015gl064364

Cisewski, B., Strass, V. H., & Leach, H. (2011). Circulation and transport of water masses in the Lazarev Sea, Antarctica, during summer and winter 2006. *Deep Sea Research Part I: Oceanographic Research Papers*, *58*(2), 186–199. https://doi.org/10.1016/j.dsr.2010.12.001

Comiso, J., & Gordon, A. (1987). Recurring polynyas over the cosmonaut sea and the maud rise. *Journal of Geophysical Research*, *92*(C3), 2819–2833. https://doi.org/10.1029/jc092ic03p02819

Copernicus Climate Change Service. (2025). ERA5 hourly time-series data on single levels from 1940 to present [Dataset]. Retrieved from https://cds.climate.copernicus.eu/datasets/reanalysis-era5-single-levels-timeseries

D'Asaro, E. A., & Lien, R.-C. (2000). The wave–turbulence transition for stratified flows. *Journal of Physical Oceanography*, *30*(7), 1669–1678. https://doi.org/10.1175/1520-0485(2000)030<1669:twttfs>2.0.co;2

De Steur, L., Holland, D., Muench, R., & Mcphee, M. G. (2007). The warm-water "halo" around maud rise: Properties, dynamics and impact. *Deep Sea Research Part I: Oceanographic Research Papers*, *54*(6), 871–896. https://doi.org/10.1016/j.dsr.2007.03.009

Dorschel, B., Hehemann, L., Viquerat, S., Warnke, F., Dreutter, S., Schulze Tenberge, Y., et al. (2022a). The international bathymetric chart of the Southern Ocean version 2 (IBCSO v2) [Dataset]. https://doi.org/10.1594/PANGAEA.937574

Dorschel, B., Hehemann, L., Viquerat, S., Warnke, F., Dreutter, S., Tenberge, Y. S., et al. (2022b). The international bathymetric chart of the Southern Ocean version 2. *Scientific Data*, *9*(1), 275. https://doi.org/10.1038/s41597-022-01366-7

Dufour, C. O., Morrison, A. K., Griffies, S. M., Frenger, I., Zanowski, H., & Winton, M. (2017). Preconditioning of the Weddell Sea polynya by the ocean mesoscale and dense water overflows. *Journal of Climate*, *30*(19), 7719–7737. https://doi.org/10.1175/jcli-d-16-0586.1

Evans, D. G., Lucas, N. S., Hemsley, V., Frajka-Williams, E., Naveira Garabato, A. C., Martin, A., et al. (2018). Annual cycle of turbulent dissipation estimated from seagliders. *Geophysical Research Letters*, *45*(19), 10–560. https://doi.org/10.1029/2018gl079966

Fahrbach, E., Hoppema, M., Rohardt, G., Schröder, M., & Wisotzki, A. (2004). Decadal-scale variations of water mass properties in the deep Weddell Sea. *Ocean Dynamics*, *54*(1), 77–91. https://doi.org/10.1007/s10236-003-0082-3

Fernández-Castro, B., Evans, D. G., Frajka-Williams, E., Vic, C., & Naveira-Garabato, A. C. (2020). Breaking of internal waves and turbulent dissipation in an anticyclonic mode water eddy. *Journal of Physical Oceanography*, *50*(7), 1893–1914. https://doi.org/10.1175/jpo-d-19-0168.1

Fernández Castro, B., Fernández Román, D., Ferron, B., Fontela, M., Lherminier, P., Naveira Garabato, A., et al. (2024). Isopycnal eddy stirring dominates thermohaline mixing in the upper subpolar north Atlantic. *Journal of Geophysical Research: Oceans*, *129*(9), e2023JC020817. https://doi.org/10.1029/2023jc020817

Ferrari, R., & Polzin, K. L. (2005). Finescale structure of the T–s relation in the eastern north Atlantic. *Journal of Physical Oceanography*, *35*(8), 1437–1454. https://doi.org/10.1175/jpo2763.1

Frajka-Williams, E., Eriksen, C. C., Rhines, P. B., & Harcourt, R. R. (2011). Determining vertical water velocities from seaglider. *Journal of Atmospheric and Oceanic Technology*, *28*(12), 1641–1656. https://doi.org/10.1175/2011jtecho830.1

Francis, D., Eayrs, C., Cuesta, J., & Holland, D. (2019). Polar cyclones at the origin of the reoccurrence of the maud rise polynya in Austral winter 2017. *Journal of Geophysical Research: Atmospheres*, *124*(10), 5251–5267. https://doi.org/10.1029/2019jd030618

Francis, D., Mattingly, K. S., Temimi, M., Massom, R., & Heil, P. (2020). On the crucial role of atmospheric Rivers in the two major weddell polynya events in 1973 and 2017 in Antarctica. *Science Advances*, *6*(46), eabc2695. https://doi.org/10.1126/sciadv.abc2695

Garau, B., Ruiz, S., Zhang, W. G., Pascual, A., Heslop, E., Kerfoot, J., & Tintoré, J. (2011). Thermal lag correction on slocum ctd glider data. *Journal of Atmospheric and Oceanic Technology*, *28*(9), 1065–1071. https://doi.org/10.1175/jtech-d-10-05030.1

Gargett, A. E. (1989). Ocean turbulence. *Annual Review of Fluid Mechanics*, *21*(1), 419–451. https://doi.org/10.1146/annurev.fl.21.010189.002223

Garrett, C. (2001). Stirring and mixing: What are the rate controlling processes. In *Proc.'aha huliko'a winter workshop* (pp. 1–8).

Golledge, N. R., Keller, E. D., Gossart, A., Malyarenko, A., Bahamondes-Dominguez, A., Krapp, M., et al. (2025). Antarctic coastal polynyas in the global climate system. *Nature Reviews Earth and Environment*, *6*(2), 1–14. https://doi.org/10.1038/s43017-024-00634-x

Gordon, A. L. (1978). Deep antarctic convection west of maud rise. *Journal of Physical Oceanography*, *8*(4), 600–612. https://doi.org/10.1175/1520-0485(1978)008<0600:dacwom>2.0.co;2

Gordon, A. L. (1991). Two stable modes of Southern Ocean winter stratification. In *Elsevier oceanography series* (Vol. 57, pp. 17–35). Elsevier.

Gordon, A. L. (2014). Southern Ocean polynya. *Nature Climate Change*, *4*(4), 249–250. https://doi.org/10.1038/nclimate2179

Gordon, A. L., Visbeck, M., & Comiso, J. C. (2007). A possible link between the weddell polynya and the southern annular mode. *Journal of Climate*, *20*(11), 2558–2571. https://doi.org/10.1175/jcli4046.1

Gülk, B., Roquet, F., Naveira Garabato, A. C., Bourdallé-Badie, R., Madec, G., & Giordani, H. (2024). Impacts of vertical convective mixing schemes and freshwater forcing on the 2016–2017 maud rise polynya openings in a regional ocean simulation. *Journal of Advances in Modeling Earth Systems*, *16*(5), e2023MS004106. https://doi.org/10.1029/2023ms004106

Gülk, B., Roquet, F., Naveira Garabato, A. C., Narayanan, A., Rousset, C., & Madec, G. (2023). Variability and remote controls of the warm-water halo and taylor cap at maud rise. *Journal of Geophysical Research: Oceans*, *128*(7), e2022JC019517. https://doi.org/10.1029/2022jc019517

Harcourt, R. R. (2005). Thermobaric cabbeling over maud rise: Theory and large eddy simulation. *Progress in Oceanography*, *67*(1–2), 186–244. https://doi.org/10.1016/j.pocean.2004.12.001

Hersbach, H., Bell, B., Berrisford, P., Hirahara, S., Horányi, A., Muñoz-Sabater, J., et al. (2020). The era5 global reanalysis. *Quarterly journal of the royal meteorological society*, *146*(730), 1999–2049. https://doi.org/10.1002/qj.3803

Holland, D. (2001). Explaining the weddell Polynya–A large ocean eddy shed at maud rise. *Science*, *292*(5522), 1697–1700. https://doi.org/10.1126/science.1059322

Jakes, M. I., Phillips, H. E., Cyriac, A., Foppert, A., Bindoff, N. L., Rintoul, S. R., & Polzin, K. L. (2025). Thermohaline interleaving in the antarctic circumpolar current. *Journal of Physical Oceanography*, *55*(3), 205–227. https://doi.org/10.1175/jpo-d-24-0048.1

Jan, S., Wang, S.-H., Yang, K.-C., Yang, Y. J., & Chang, M.-H. (2019). Glider observations of interleaving layers beneath the kuroshio primary velocity core east of Taiwan and analyses of underlying dynamics. *Scientific Reports*, *9*(1), 11401. https://doi.org/10.1038/s41598-019-47912-z

Kjellsson, J., Holland, P. R., Marshall, G. J., Mathiot, P., Aksenov, Y., Coward, A. C., et al. (2015). Model sensitivity of the weddell and ross seas, Antarctica, to vertical mixing and freshwater forcing. *Ocean Modelling*, *94*, 141–152. https://doi.org/10.1016/j.ocemod.2015.08.003

Klocker, A., & Abernathey, R. (2014). Global patterns of mesoscale eddy properties and diffusivities. *Journal of Physical Oceanography*, *44*(3), 1030–1046. https://doi.org/10.1175/jpo-d-13-0159.1

Kolmogorov, A. N. (1991). The local structure of turbulence in incompressible viscous fluid for very large Reynolds numbers. *Proceedings of the Royal Society of London. Series A: Mathematical and Physical Sciences*, *434*(1890), 9–13. https://doi.org/10.1098/rspa.1991.0075

Kurtakoti, P., Veneziani, M., Stössel, A., & Weijer, W. (2018). Preconditioning and formation of maud rise polynyas in a high-resolution Earth system model. *Journal of Climate*, *31*(23), 9659–9678. https://doi.org/10.1175/jcli-d-18-0392.1

Kuzmina, N., Rudels, B., Stipa, T., & Zhurbas, V. (2005). The structure and driving mechanisms of the Baltic intrusions. *Journal of Physical Oceanography*, *35*(6), 1120–1137. https://doi.org/10.1175/jpo2749.1

Large, W. G., & Pond, S. (1981). Open ocean momentum flux measurements in moderate to strong winds. *Journal of Physical Oceanography*, *11*(3), 324–336. https://doi.org/10.1175/1520-0485(1981)011<0324:oomfmi>2.0.co;2

Leach, H., Strass, V., & Cisewski, B. (2011). Modification by lateral mixing of the warm deep water entering the Weddell Sea in the maud rise region. *Ocean Dynamics*, *61*(1), 51–68. https://doi.org/10.1007/s10236-010-0342-y

Martin, T., Park, W., & Latif, M. (2013). Multi-centennial variability controlled by Southern Ocean convection in the kiel climate model. *Climate Dynamics*, *40*(7), 2005–2022. https://doi.org/10.1007/s00382-012-1586-7

Martinson, D. G., Killworth, P. D., & Gordon, A. L. (1981). A convective model for the weddell polynya. *Journal of Physical Oceanography*, *11*(4), 466–488. https://doi.org/10.1175/1520-0485(1981)011<0466:acmftw>2.0.co;2

May, B. D., & Kelley, D. E. (1997). Effect of baroclinicity on double-diffusive interleaving. *Journal of Physical Oceanography*, *27*(9), 1997–2008. https://doi.org/10.1175/1520-0485(1997)027<1997:eobodd>2.0.co;2

May, B. D., & Kelley, D. E. (2001). Growth and steady state stages of thermohaline intrusions in the Arctic Ocean. *Journal of Geophysical Research*, *106*(C8), 16783–16794. https://doi.org/10.1029/2000jc000605

McDougall, T. J., & Barker, P. M. (2011). Getting started with teos-10 and the Gibbs seawater (gsw) oceanographic toolbox. *Scor/iapso WG*, *127*(532), 1–28.

McGraw, K., Morley, A., & Ward, B. (2025). High-latitude cabbeling observations along the east Greenland polar front. *Journal of Geophysical Research: Oceans*, *130*(7), e2025JC022567. https://doi.org/10.1029/2025jc022567

Mohrmann, M., Heuzé, C., & Swart, S. (2021). Southern ocean polynyas in cmip6 models. *The Cryosphere*, *15*(9), 4281–4313. https://doi.org/10.5194/tc-15-4281-2021

Mohrmann, M., Swart, S., & Heuzé, C. (2022). Observed mixing at the flanks of maud rise in the weddell sea. *Geophysical Research Letters*, *49*(8), e2022GL098036. https://doi.org/10.1029/2022gl098036

Morioka, Y., Zhang, L., Cooke, W., Nonaka, M., Behera, S. K., & Manabe, S. (2024). Role of anthropogenic forcing in antarctic sea ice variability simulated in climate models. *Nature Communications*, *15*(1), 10511. https://doi.org/10.1038/s41467-024-54485-7

Moum, J. N. (1996). Energy-containing scales of turbulence in the ocean thermocline. *Journal of Geophysical Research*, *101*(C6), 14095–14109. https://doi.org/10.1029/96jc00507

Muench, R., Morison, J., Padman, L., Martinson, D., Schlosser, P., Huber, B., & Hohmann, R. (2001). Maud rise revisited. *Journal of Geophysical Research*, *106*(C2), 2423–2440. https://doi.org/10.1029/2000jc000531

Narayanan, A., Roquet, F., Gille, S. T., Gülk, B., Mazloff, M. R., Silvano, A., & Naveira Garabato, A. C. (2024). Ekman-driven salt transport as a key mechanism for open-ocean polynya formation at maud rise. *Science Advances*, *10*(18), eadj0777. https://doi.org/10.1126/sciadv.adj0777

Neme, J., England, M. H., & Hogg, A. M. (2021). Seasonal and interannual variability of the weddell gyre from a high-resolution global ocean-sea ice simulation during 1958–2018. *Journal of Geophysical Research: Oceans*, *126*(11), e2021JC017662. https://doi.org/10.1029/2021jc017662

Osborn, T. R. (1980). Estimates of the local rate of vertical diffusion from dissipation measurements. *Journal of Physical Oceanography*, *10*(1), 83–89. https://doi.org/10.1175/1520-0485(1980)010<0083:eotlro>2.0.co;2

Parkinson, C. L. (2019). A 40-y record reveals gradual antarctic sea ice increases followed by decreases at rates far exceeding the rates seen in the arctic. *Proceedings of the National Academy of Sciences*, *116*(29), 14414–14423. https://doi.org/10.1073/pnas.1906556116

Purich, A., & Doddridge, E. W. (2023). Record low antarctic sea ice coverage indicates a new sea ice state. *Communications Earth and Environment*, *4*(1), 314. https://doi.org/10.1038/s43247-023-00961-9

Qin, Q., Wang, Z., Liu, C., & Cheng, C. (2022). Open-ocean polynyas in the cooperation sea, Antarctica. *Journal of Physical Oceanography*, *52*(7), 1363–1381. https://doi.org/10.1175/jpo-d-21-0197.1

Rheinlænder, J. W., Smedsrud, L. H., & Nisancioglu, K. H. (2021). Internal ocean dynamics control the long-term evolution of weddell Sea polynya activity. *Frontiers in Climate*, *3*, 718016. https://doi.org/10.3389/fclim.2021.718016

Ruddick, B. R., & Kerr, O. (2003). Oceanic thermohaline intrusions: Theory. *Progress in Oceanography*, *56*(3–4), 483–497. https://doi.org/10.1016/s0079-6611(03)00029-6

Ruddick, B. R., Phillips, O. M., & Turner, J. S. (1999). A laboratory and quantitative model of finite-amplitude thermohaline intrusions. *Dynamics of Atmospheres and Oceans*, *30*(2–4), 71–99. https://doi.org/10.1016/s0377-0265(99)00021-4

Schmitt, R. W. (1994). Double diffusion in oceanography. *Annual Review of Fluid Mechanics*, *26*(1), 255–285. https://doi.org/10.1146/annurev.fl.26.010194.001351

Shaw, W. J., & Stanton, T. P. (2014). Dynamic and double-diffusive instabilities in a weak pycnocline. Part I: Observations of heat flux and diffusivity in the vicinity of maud rise, Weddell Sea. *Journal of Physical Oceanography*, *44*(8), 1973–1991. https://doi.org/10.1175/jpo-d-13-042.1

Shcherbina, A. Y., Gregg, M. C., Alford, M. H., & Harcourt, R. R. (2009). Characterizing thermohaline intrusions in the north Pacific subtropical frontal zone. *Journal of Physical Oceanography*, *39*(11), 2735–2756. https://doi.org/10.1175/2009jpo4190.1

Silvano, A., Narayanan, A., Catany, R., Olmedo, E., González-Gambau, V., Turiel, A., et al. (2025). Rising surface salinity and declining sea ice: A new Southern Ocean state revealed by satellites. *Proceedings of the National Academy of Sciences*, *122*(27), e2500440122. https://doi.org/10.1073/pnas.2500440122

Silvano, A., Purkey, S., Gordon, A. L., Castagno, P., Stewart, A. L., Rintoul, S. R., et al. (2023). Observing antarctic bottom water in the Southern Ocean. *Frontiers in Marine Science*, *10*, 1221701. https://doi.org/10.3389/fmars.2023.1221701

Smith, K. S., & Ferrari, R. (2009). The production and dissipation of compensated thermohaline variance by mesoscale stirring. *Journal of Physical Oceanography*, *39*(10), 2477–2501. https://doi.org/10.1175/2009jpo4103.1

SO-CHIC consortium, Sallée, J., Abrahamsen, E., Allaigre, C., Auger, M., Ayres, H., et al. (2023). Southern Ocean carbon and heat impact on climate. *Philosophical Transactions of the Royal Society A*, *381*(2249), 20220056. https://doi.org/10.1098/rsta.2022.0056

Spence, P., Menviel, L., Morrison, A. K., Foppert, A., & Silvano, A. (2025). On the relationship between the weddell polynya and antarctic bottom water trends. *Journal of Climate*, *38*(24), 7249–7268. https://doi.org/10.1175/jcli-d-24-0179.1

Spira, T., Swart, S., Giddy, I., & du Plessis, M. (2024). The observed spatiotemporal variability of antarctic winter water. *Journal of Geophysical Research: Oceans*, *129*(10), e2024JC021017. https://doi.org/10.1029/2024jc021017

Stoessel, A., Notz, D., Haumann, F. A., Haak, H., Jungclaus, J., & Mikolajewicz, U. (2015). Controlling high-latitude Southern ocean convection in climate models. *Ocean Modelling*, *86*, 58–75.

Swart, S., du Plessis, M., Giddy, I., Edholm, J., Spira, T., Biddle, L., & Rosenthal, H. S. (2025). Dataset from autonomous assets collected during the SO-CHIC field campaign in the southern ocean [Dataset]. https://doi.org/10.5281/zenodo.15228200

Taylor, G. I. (1923). Experiments on the motion of solid bodies in rotating fluids. *Proceedings of the Royal Society of London - Series A: Containing Papers of a Mathematical and Physical Character*, *104*(725), 213–218. https://doi.org/10.1098/rspa.1923.0103

Tennekes, H., & Lumley, J. L. (1972). *A first course in turbulence*. MIT press.

Testor, P., Bosse, A., Houpert, L., Margirier, F., Mortier, L., Legoff, H., et al. (2018). Multiscale observations of deep convection in the northwestern mediterranean Sea during winter 2012–2013 using multiple platforms. *Journal of Geophysical Research: Oceans*, *123*(3), 1745–1776. https://doi.org/10.1002/2016jc012671 van Westen, R. M., & Dijkstra, H. A. (2020). Multidecadal preconditioning of the maud rise polynya region. *Ocean Science*, *16*(6), 1443–1457. https://doi.org/10.5194/os-16-1443-2020

Vernet, M., Geibert, W., Hoppema, M., Brown, P. J., Haas, C., Hellmer, H. H., et al. (2019). The weddell gyre, Southern Ocean: Present knowledge and future challenges. *Reviews of Geophysics*, *57*(3), 623–708. https://doi.org/10.1029/2018rg000604

Wadhams, P. (2014). *Ice in the ocean*. CRC Press.

Wang, X. (2026). Code and supporting data for "Preconditioning of polynya formation by ocean mixing at Maud Rise, Antarctica" [Software]. https://doi.org/10.5281/zenodo.19810990

Wang, Z., Wu, Y., Lin, X., Liu, C., & Xie, Z. (2017). Impacts of open-ocean deep convection in the Weddell Sea on coastal and bottom water temperature. *Climate Dynamics*, *48*(9–10), 2967–2981. https://doi.org/10.1007/s00382-016-3244-y

Wei, Z., Zhang, Z., Wang, X., Chen, Y., & Zhou, M. (2022). The thermodynamic and dynamic control of the sensible heat polynya in the Western cosmonaut sea. *Deep Sea Research Part II: Topical Studies in Oceanography*, *195*, 105000. https://doi.org/10.1016/j.dsr2.2021.105000

Zanowski, H., & Hallberg, R. (2017). Weddell polynya transport mechanisms in the abyssal ocean. *Journal of Physical Oceanography*, *47*(12), 2907–2925. https://doi.org/10.1175/jpo-d-17-0091.1

Zanowski, H., Hallberg, R., & Sarmiento, J. L. (2015). Abyssal ocean warming and salinification after weddell polynyas in the gfdl cm2g coupled climate model. *Journal of Physical Oceanography*, *45*(11), 2755–2772. https://doi.org/10.1175/jpo-d-15-0109.1

Zhou, L., Ayres, H., Gülk, B., Narayanan, A., de Lavergne, C., Ödalen, M., et al. (2026). Weddell Sea polynya formation, cessation and climatic impacts. *The Cryosphere*, *20*(1), 285–308. https://doi.org/10.5194/tc-20-285-2026

Zhou, L., Heuzé, C., & Mohrmann, M. (2023). Sea ice production in the 2016 and 2017 maud rise polynyas. *Journal of Geophysical Research: Oceans*, *128*(2), e2022JC019148. https://doi.org/10.1029/2022jc019148